Astronomy & Astrophysics manuscript no. TOI-396
December 11, 2024

©ESO 2024

Radii, masses, and transit-timing variations of the three-planet system orbiting the naked-eye star TOI-396[⋆]

A. Bonfanti[1], I. Amateis[2,1,3], D. Gandolfi[2], L. Borsato[4], J. A. Egger[5], P. E. Cubillos[1,6], D. Armstrong[7,8], I. C. Leão[9], M. Fridlund[10,11], B. L. Canto Martins[9,12], S. G. Sousa[13], J. R. De Medeiros[9], L. Fossati[1], V. Adibekyan[13], A. Collier Cameron[14], S. Grziwa[15], K. W. F. Lam[16], E. Goffo[17], L. D. Nielsen[18], F. Rodler[19], J. Alarcon[20], J. Lillo-Box[21], W. D. Cochran[22,23], R. Luque[24], S. Redfield[25], N. C. Santos[13,26], S. C. C. Barros[13,26], D. Bayliss[7,8], X. Dumusque[27], M. A. F. Keniger[7,8], J. Livingston[28,29,30], F. Murgas[31,32], G. Nowak[33], A. Osborn[34], H. P. Osborn[5,35], E. Pallé[31,32], C. M. Persson[11], L. M. Serrano[2], P. A. Strøm[7,8], S. Udry[27], and P. J. Wheatley[7,8]

(Affiliations can be found after the references)

ABSTRACT

Context. TOI-396 is an F6 V bright naked-eye star ($V \approx 6.4$) orbited by three small ($R_p \approx 2\,R_\oplus$) transiting planets discovered thanks to space-based photometry from two *TESS* sectors. The orbital periods of the two innermost planets, namely TOI-396 b and c, are close to the 5:3 commensurability ($P_b \sim 3.6$ d and $P_c \sim 6.0$ d), suggesting that the planets might be trapped in a mean motion resonance (MMR).
Aims. To measure the masses of the three planets, refine their radii, and investigate whether planets b and c are in MMR, we carried out *HARPS* radial velocity (RV) observations of TOI-396 and retrieved archival high-precision transit photometry from four *TESS* sectors.
Methods. We extracted the RVs via a skew-normal fit onto the *HARPS* cross-correlation functions and performed a Markov chain Monte Carlo joint analysis of the Doppler measurements and transit photometry while employing the breakpoint method to remove stellar activity from the RV time series. We also performed a transit timing variation (TTV) dynamical analysis of the system and simulated the temporal evolution of the TTV amplitudes of the three planets following an N-body numerical integration.
Results. Our analysis confirms that the three planets have similar sizes ($R_b = 2.004^{+0.045}_{-0.047}\,R_\oplus$; $R_c = 1.979^{+0.054}_{-0.051}\,R_\oplus$; $R_d = 2.001^{+0.063}_{-0.064}\,R_\oplus$) and is thus in agreement with previous findings. However, our measurements are ~ 1.4 times more precise thanks to the use of two additional *TESS* sectors. For the first time, we have determined the RV masses for TOI-396 b and d, finding them to be $M_b = 3.55^{+0.94}_{-0.96}\,M_\oplus$ and $M_d = 7.1 \pm 1.6\,M_\oplus$, which implies bulk densities of $\rho_b = 2.44^{+0.69}_{-0.68}$ g cm^{-3} and $\rho_d = 4.9^{+1.2}_{-1.1}$ g cm^{-3}, respectively. Our results suggest a quite unusual system architecture, with the outermost planet being the densest. Based on a frequency analysis of the *HARPS* activity indicators and *TESS* light curves, we find the rotation period of the star to be $P_{\mathrm{rot},\star} = 6.7 \pm 1.3$ d, in agreement with the value predicted from $\log R'_{\mathrm{HK}}$-based empirical relations. The Doppler reflex motion induced by TOI-396 c remains undetected in our RV time series, likely due to the proximity of the planet's orbital period to the star's rotation period. We also discovered that TOI-396 b and c display significant TTVs. While the TTV dynamical analysis returns a formally precise mass for TOI-396 c of $M_{c,\mathrm{dyn}} = 2.24^{+0.13}_{-0.67}\,M_\oplus$, the result might not be accurate, owing to the poor sampling of the TTV phase. We also conclude that TOI-396 b and c are close to but out of the 5:3 MMR.
Conclusions. A TTV dynamical analysis of additional transit photometry evenly covering the TTV phase and super-period is likely the most effective approach for precisely and accurately determining the mass of TOI-396 c. Our numerical simulation suggests TTV semi-amplitudes of up to 5 hours over a temporal baseline of ~ 5.2 years, which should be duly taken into account when scheduling future observations of TOI-396.

Key words. planets and satellites: fundamental parameters – stars: fundamental parameters – techniques: photometric – techniques: radial velocities

1. Introduction

Multi-planet systems enable us to place significantly stronger constraints on formation and evolution mechanisms compared to single-planet systems (e.g. Lissauer et al. 2011; Fabrycky et al. 2014; Winn & Fabrycky 2015; Mishra et al. 2023). As a matter of fact, the temporal evolution of the gas content in the proto-planetary disc influences planet migration (e.g. Lin & Papaloizou 1979; Goldreich & Tremaine 1980; Tanaka et al. 2002; D'Angelo & Lubow 2008; Alexander & Armitage 2009), which shapes the orbital architecture of a planetary system. The latter is further expected to correlate with the planet composition (e.g.

Thiabaud et al. 2014, 2015; Walsh et al. 2015; Bergner et al. 2020; Li et al. 2020) that can be inferred once the physical parameters of the planets are known (e.g. Dorn et al. 2017; Otegi et al. 2020b; Leleu et al. 2021; Haldemann et al. 2024).

If planets are found in mean motion resonance (MMR; e.g. Lee & Peale 2002; Correia et al. 2018), systems can also shed light on the migration mechanisms during formation, as well as on the impact of tidal effects occurring later on (e.g. Delisle et al. 2012; Izidoro et al. 2017). In addition, planets in, or close to, MMR likely exhibit transit timing variations (TTVs; see e.g. Agol et al. 2005; Agol & Fabrycky 2018; Leleu et al. 2021) that enable one to infer planetary masses without necessarily relying on radial velocity (RV) measurements, which are not always possible (e.g. Hatzes 2016).

Multi-planet systems also give insights into correlations between physical and orbital parameters of exoplanets. For example, Weiss et al. (2018) noticed that planets in adjacent orbits usually show similar radii, hence the "peas in a pod" label to describe this scenario. Weiss et al. (2018) further noticed that the outermost planet is the largest in the majority of cases, which agrees with the observed bulk planet density (ρ_p) trend highlighted by Mishra et al. (2023), where ρ_p decreases with the distance from the stellar host as outer planets are expected to be richer in volatiles (thus bigger and less dense).

The object TOI-396 represents an interesting laboratory to test these theories as it is the brightest star known so far to host three transiting planets (Vanderburg et al. 2019) after ν^2 Lupi (Delrez et al. 2021). After analysing two sectors from the Transiting Exoplanet Survey Satellite (*TESS*; Ricker et al. 2015), Vanderburg et al. (2019) found that the three planets have radii of ∼ $2 R_\oplus$ and orbital periods of ∼ 3.6, ∼ 6.0, and ∼ 11.2 d, with TOI-396 c and b showing a period commensurability close to the 5:3 ratio. Following the notation introduced in Mishra et al. (2023), the three planets are 'similar' in terms of radii, and one may wonder whether this architecture class is kept also in the mass-period diagram. Mishra et al. (2023) found a positive and strong correlation of the coefficients of similarity between radii and masses, though exceptions are possible (e.g. Weiss & Marcy 2014; Otegi et al. 2020a, 2022).

In this work, we complement the photometric analysis of new *TESS* light curves (LCs) with RV observations taken with the High Accuracy Radial Velocity Planet Searcher (*HARPS*; Mayor et al. 2003) spectrograph to refine the planet radii and constrain for the first time the planetary masses. Considering the possible 5:3 MMR between TOI-396 c and b, we also simulate the evolution in time of the TTV amplitudes. This paper is organised as follows: Section 2 presents the stellar properties, and Sect. 3 describes the photometric and RV data. After outlining the method to jointly analyse the *TESS* LCs and the *HARPS* RV time series in Sect. 4, we present the corresponding results in Sect. 5. We attempt to dynamically model TTV and RV data simultaneously and track the temporal evolution of the TTV signals in Sect. 6, and we study the planets' internal structure in Sect. 7 and explore the prospects for characterising the system with the James Webb Space Telescope (JWST; Gardner et al. 2006) in Sect. 8. Finally Sect. 9 gathers the conclusions.

2. Host star characterisation

TOI-396 is an F6 V (Gray et al. 2006) bright naked-eye star with an apparent visual magnitude of $V \approx 6.4$ (Perryman et al. 1997). It is located ∼ 31.7 pc away and is visible in the constellation of Fornax in the southern hemisphere. It is member of a visual binary system and its companion HR 858 B is a faint M-dwarf ($G \sim 16$ mag), about 8.4″ away from the main component.

We co-added 78 *HARPS* spectra (see Sect. 3.2 for further details) and then modelled it with Spectroscopy Made Easy[1] (SME; Piskunov & Valenti 2017) version 5.2.2. SME computes synthetic spectra from a grid of well established stellar atmosphere models and adjusts a chosen free parameter based on comparison with the observed spectrum. Here we used the stellar atmosphere grid Atlas12 (Kurucz 2013) together with atomic line lists from the Vald database (Piskunov et al. 1995) in order to produce the synthetic spectra. We modelled one parameter at a time utilising spectral features sensitive to different photospheric parameters iterating until convergence of all free parameters. Throughout

the modelling, we held the macro- and micro-turbulent velocities, v_{mac} and v_{mic}, fixed to 6 km s^{-1} (Doyle et al. 2014) and 1.34 km s^{-1} (Bruntt et al. 2010), respectively. A description of the modelling procedure is detailed in Persson et al. (2018). Finally, we obtained T_{eff} = 6354 ± 70 K, [Fe/H] = 0.025 ± 0.050, $\log g$ = 4.30 ± 0.06, and $v \sin i_\star$ = 7.5 ± 0.2 km s^{-1}.

To double-check the derived spectroscopy parameters we performed an additional analysis employing ARES+MOOG (Sousa et al. 2021; Sousa 2014; Santos et al. 2013). In detail, we used the latest version of ARES [2] (Sousa et al. 2007, 2015) to consistently measure the equivalent widths (EW) for the list of iron lines presented in Sousa et al. (2008). Following a minimisation process, we then find the ionisation and excitation equilibria to converge for the best set of spectroscopic parameters. This process uses a grid of Kurucz model atmospheres (Kurucz 1993) and the radiative transfer code MOOG (Sneden 1973). We obtained T_{eff} = 6389 ± 67 K, [Fe/H] = −0.014 ± 0.045 dex, $\log g$ = 4.58 ± 0.11, and v_{mic} = 1.54 ± 0.04 km s^{-1}. In this process we also derived a more accurate trigonometric surface gravity ($\log g_{trig}$ = 4.34 ± 0.02) using recent GAIA data following the same procedure as described in Sousa et al. (2021). In the end ARES+MOOG provides consistent values when compared with the ones derived with SME.

Using the SME stellar atmospheric parameters, we determined the abundances of Mg and Si following the classical curve-of-growth analysis method described in Adibekyan et al. (2012, 2015). Similar to the stellar parameter determination, we used ARES to measure the EWs of the spectral lines of these elements and a grid of Kurucz model atmospheres (Kurucz 1993) along with the radiative transfer code MOOG to convert the EWs into abundances, assuming local thermodynamic equilibrium.

The stellar radius $R_\star$, mass $M_\star$, and age $t_\star$ were derived homogeneously using the isochrone placement algorithm (Bonfanti et al. 2015, 2016) and its capability of interpolating a flexible set of input parameters within pre-computed grids of PARSEC[3] v1.2S (Marigo et al. 2017) isochrones and tracks. For each magnitude listed in Table 1, we performed an isochrone placement run by inserting the spectroscopic parameters derived above, the Gaia parallax π (Gaia Collaboration et al. 2023, offset-corrected following Lindegren et al. 2021), and the magnitude value to obtain an estimate for the stellar radius, mass, and age along with their uncertainties. From these results, we built the corresponding Gaussian probability density functions (PDFs) and then we merged (i.e. we summed) the PDFs derived from the different runs to obtain robust estimates for $R_\star$, $M_\star$, and $t_\star$. The radius $R_\star$ derives essentially from T_{eff}, π, and the stellar magnitude, while $M_\star$ and $t_\star$ are much more model-dependent; therefore we conservatively inflated their internal uncertainties by 4% and 20%, respectively, following Bonfanti et al. (2021). Our adopted stellar parameters are listed in Table 1.

3. Observational data

3.1. TESS photometry

As presented in Vanderburg et al. (2019), TOI-396 was photometrically monitored by *TESS* during the first year of its nominal mission in Sector 3 from 20 September to 17 October 2018 (UT) in CCD 2 of Camera 2, and in Sector 4 from 19 October to 14 November 2018 (UT) in CCD 2 of Camera 1. TOI-396 was later

---

[1] http://www.stsci.edu/~valenti/sme.html.

[2] The last version, ARES v2, can be downloaded at https://github.com/sousasag/ARES.

[3] http://stev.oapd.inaf.it/cgi-bin/cmd.

Table 1: Stellar properties of TOI-396.

Star names	TOI-396	
	TIC 178155732	
	HR 858	
	HD 17926	
	HIP 13363	
	Gaia DR3 5064574724769475968	

Parameter	Value	Source
RA [h:min:s]	02:51:56.25	Gaia DR3
Dec [°:′:″]	−30:48:52.26	Gaia DR3
B	6.862 ± 0.015	Perryman et al. (1997)
V	6.382 ± 0.010	Perryman et al. (1997)
B_T	6.956 ± 0.015	Høg et al. (2000)
V_T	6.438 ± 0.010	Høg et al. (2000)
J	5.473 ± 0.027	Cutri et al. (2003)
H	5.225 ± 0.034	Cutri et al. (2003)
K	5.149 ± 0.020	Cutri et al. (2003)
G	6.2650 ± 0.0028	Gaia DR3
G_{RP}	6.5100 ± 0.0029	Gaia DR3
G_{BP}	5.8555 ± 0.0038	Gaia DR3
π [mas]	31.564 ± 0.035	Gaia DR3[a]
$T_{\rm eff}$ [K]	6354 ± 70	Spectroscopy
[Fe/H]	0.025 ± 0.050	Spectroscopy
[Mg/H]	-0.01 ± 0.07	Spectroscopy
[Si/H]	-0.03 ± 0.05	Spectroscopy
$\log g$ [cgs]	4.30 ± 0.06	Spectroscopy
$v \sin i_\star$ [km s^{-1}]	7.5 ± 0.2	Spectroscopy
$\log R'_{\rm HK}$	-4.926 ± 0.014	Spectroscopy
$P_{\rm rot,\star}$ [d]	6.7 ± 1.3	$\log R'_{\rm HK}$
$R_\star$ [$R_\odot$]	1.258 ± 0.019	π & photometry[b]
$M_\star$ [$M_\odot$]	1.204 ± 0.052	Isochrones
$t_\star$ [Gyr]	2.0 ± 0.6	Isochrones
$L_\star$ [$L_\odot$]	2.31 ± 0.12	From $T_{\rm eff}$ & $R_\star$
$\rho_\star$ [$\rho_\odot$]	0.605 ± 0.038	From $M_\star$ & $R_\star$

Notes. RA & DEC are reported as in J2000 reference frame. Values in the bottom half of the table have been derived as part of this paper.
[a] Zero-point correction from Lindegren et al. (2021) applied.
[b] $R_\star$ is computed within the isochrone placement interpolation scheme as PARSEC isochrones convert stellar luminosity into absolute magnitudes via a series of bolometric correction tables built as explained in Marigo et al. (2017) and references therein.

re-observed by *TESS* during the first year of its extended mission in Sector 30 from 23 September to 20 October 2020 (UT) in CCD 2 of Camera 2, and in Sector 31 from 22 October to 16 November 2020 (UT) in CCD 2 of Camera 1. All data were collected at a 2-minute cadence, except for Sector 3 for which *TESS* only sent down data at 30-minute cadence.

We analyse all available *TESS* time series, including the Sector 3 and 4 data already presented in (Vanderburg et al. 2019). For Sector 3 we used the *TESS* Asteroseismic Science Opera-

tion Center (TASOC) photometry (Handberg et al. 2021; Lund et al. 2021), while for the other sectors we analysed the Presearch Data Conditioning Simple Aperture Photometry (PDC-SAP) LCs generated by the *TESS* Science Processing Operation Center (SPOC) pipeline Jenkins et al. (2016), which removes the majority of instrumental artefacts and systematic trends (Smith et al. 2012; Stumpe et al. 2012, 2014). We rejected those data marked with a bad quality flag and we performed a 5 median-absolute-deviation (MAD) clipping of flux data points. After that, we built our custom LCs by splitting the *TESS* sectors in temporal windows centred around the transit events keeping ~ 4 h of out-of-transit data points both before and after the transit for de-trending purposes. We ended up with 41 *TESS* LCs reporting the epoch of observation (t), the flux and its error, and further ancillary vectors available from the *TESS* science data product, that is MOM_CENTR1, MOM_CENTR2 (hereafter denoted with x and y, respectively), POS_CORR1, and POS_CORR2 (hereafter denoted with pc1 and pc2, respectively)[4].

3.2. HARPS high-resolution spectroscopy

We performed the radial velocity (RV) follow-up of TOI-396 with the *HARPS* spectrograph mounted at the ESO-3.6 m telescope at La Silla Observatory (Chile). We acquired 77 high resolution ($R \approx 115\,000$) spectra between 31 January and 27 July 2019 (UT), covering a baseline of ~ 177 days, as part of the follow-up programs of *TESS* systems carried out with the *HARPS* spectrograph (IDs: 1102.C-0923, 1102.C-0249, 0102.C-0584; PIs: Gandolfi, Armstrong, De Medeiros). One additional spectrum was acquired during a technical night (ID: 60.A-9700) in February 2019. Following Dumusque et al. (2011b), we averaged out p-mode stellar pulsations by setting the exposure time to 900 s, which led to a median signal-to-noise (S/N) ratio of ~320 per pixel at 550 nm. We used the second fibre of the *HARPS* spectrograph to simultaneously observe a Fabry-Perot lamp and trace possible instrumental drift down to the sub-metre per second level (Wildi et al. 2010). We reduced the data using the dedicated *HARPS* data reduction software (DRS; Pepe et al. 2002; Lovis, C. & Pepe, F. 2007) and computed the cross-correlation function (CCF) for each spectrum using a G2 numerical mask (Baranne et al. 1996).

We then performed a skew-normal (SN) fit on each CCF (Simola et al. 2019) in order to extract the stellar radial velocity along with its error, the full width at half maximum (FWHM$_{\rm SN}$), the contrast (A), and the skewness parameter (γ) of the CCF. The advantages of using an SN-fit rather than a Normal fit are thoroughly discussed in Simola et al. (2019), while the SN-fitting details are outlined in, for example, Bonfanti et al. (2023); Luque et al. (2023); Fridlund et al. (2024). After the SN-based extraction, we ended up with an RV time series, whose ancillary vectors (FWHM$_{\rm SN}$, A, γ) are the activity indicators used to constrain the polynomial basis to model and de-trend the RV component of the stellar activity (see Table A.1).

As stellar activity is not stationary, the correlations between the RV observations and the activity indicators are expected to change over time as discussed in Simola et al. (2022), who proposed to apply the breakpoint (*bp*) technique (Bai & Perron 2003) to check whether these correlation changes are statistically significant. If so, the *bp* algorithm finds the optimal locations of correlation changes, which defines the segmenta-

---

[4] Please refer to https://tasoc.dk/docs/EXP-TESS-ARC-ICD-TM-0014-Rev-F.pdf for further details about the output of the *TESS* science data products.

tion characterised by the lowest Bayesian Information Criterion (BIC; Schwarz 1978). Indeed, we found one breakpoint at observation 48 (BJD = 2458667.940719; ΔBIC ≈ −14 with respect to the zero-breakpoint solution). Thus, we split our RV time series in two piecewise stationary segments and de-trended it on a chunk-wise base, rather than performing a global de-trending over the whole time series, similarly to what has already been done in Bonfanti et al. (2023); Luque et al. (2023).

4. Methods

We jointly analysed the *TESS* LCs and the RV time series within a Markov chain Monte Carlo (MCMC) framework using the MCMCI code (Bonfanti & Gillon 2020). When fitting the *TESS* LCs extracted from Sector 3 that has a cadence of 30 min, we generated the transit model using a cadence of 2 min (the same as the other *TESS* sectors) and then rebinned it to 30 min following Kipping (2010), who warns that long-cadence photometry may lead to retrieve erroneous system parameters. We imposed Normal priors on the input stellar parameters (i.e. $T_{\rm eff}$, [Fe/H], $R_\star$, and $M_\star$), as derived in Sect. 2 with a twofold aim: (i) the induced prior on the mean stellar density $\rho_\star$ (via $M_\star$ and $R_\star$) helps the convergence of the transit model; (ii) limb darkening (LD) coefficients for the *TESS* filter may be retrieved following interpolation within ATLAS9-based[5] grids that were precomputed using the `get_lds.py` code[6] by Espinoza & Jordán (2015). We then set Normal priors on the quadratic LD coefficients using the values coming from the grid interpolation (i.e. $u_{1,TESS} = 0.2318 \pm 0.0065$ and $u_{2,TESS} = 0.3085 \pm 0.0028$) after re-parameterising them following Holman et al. (2006). On the planetary side, we adopted unbounded (except for the physical limits) uniform priors on the transit depth dF, the impact parameter b, the orbital period P, the transit timing T_0, and the RV semi-amplitude K, while we set the eccentricity $e = 0$ and the argument of periastron $\omega = 90°$ for all planets. We come back to the assumption on the eccentricity below. The specific parameterisations of the jump parameters (aka step parameters) are outlined in Bonfanti & Gillon (2020).

The LCs and the RV time series were de-trended simultaneously during the MCMC analysis using polynomials. To assess the polynomial orders to be associated with the different de-trending parameters for each time series, we first launch several MCMC preliminary runs made of 10 000 steps where we varied only one polynomial order at a time. We then selected the best de-trending baseline (see Table A.2) as the one having the lowest BIC. After that, we performed a preliminary MCMCI run comprising 200 000 steps to evaluate the contribution of both the white and red noise in the LCs following Pont et al. (2006); Bonfanti & Gillon (2020), so to properly rescale the photometric errors and get reliable uncertainties on the output parameters. Finally, three independent MCMCI runs comprising 200 000 steps each (burn-in length equal to 20%) were performed to build the posterior distributions of the output parameters after checking their convergence via the Gelman-Rubin statistic ($\hat{R}$; Gelman & Rubin 1992).

We also tested the possibility of eccentric orbits by imposing uniform priors on ($\sqrt{e}\cos\omega$, $\sqrt{e}\cos\omega$) either bounded to imply $e \lesssim 0.3$ or completely unbounded (except for the physical limits). The wider the eccentricity range to be explored by the MCMC scheme, the poorer the parameter convergence, which suggests that the available data are not enough to con-

strain the planetary eccentricities well. Moreover, the MCMCI runs with $e \neq 0$ are disfavoured by the ΔBIC criterion (e.g. Kass & Raftery 1995; Trotta 2007) as well, in fact we obtained $\Delta BIC = BIC_{e\neq0} - BIC_{e=0} \gtrsim +100$. This is also in agreement with the simulations performed by Vanderburg et al. (2019), who suggested that the periods' commensurability state of planets b and c is more likely maintained if the system is characterised by low eccentricities. Therefore, we adopted the circular solution as the reference one.

5. LC and RV data analysis results

5.1. Joint LC and RV analysis with linear ephemerides

As mentioned in Sect. 4, we set P and T_0 as free parameters under the control of a uniform prior, which implies assuming linear ephemerides. With this setup, we improved the transit depth precision of all three planets by a factor ∼ 1.4 if compared with the results of Vanderburg et al. (2019). This improvement level is consistent with having twice the number of data points with respect to the LC analysis performed by Vanderburg et al. (2019), as well as with low TTV amplitudes (see Sect. 5.2).

By combining the SN-fit onto the *HARPS* CCFs along with the *bp* method, we were able to estimate the masses of TOI-396 b and TOI-396 d to $M_b = 3.56^{+0.92}_{-0.94}\,M_\oplus$ and $M_d = 7.2 \pm 1.6\,M_\oplus$ (detections at the 3.8 and 4.5σ-level, respectively). Instead, we did not detect any significant Keplerian signal at the orbital period of TOI-396 c within the RV time series. In detail, we obtained a median $K_c = 0.28^{+0.29}_{-0.20}$ m s^{-1} (3σ upper limit $K_c^{\rm up} = 1.2$ m s^{-1}), which implies $M_c = 0.92^{+0.94}_{-0.63}\,M_\oplus$ ($M_c^{\rm up} = 4.0\,M_\oplus$).

When combining the mass and radius values of the three planets, we obtain the following median estimates for the bulk planetary densities: $\rho_b = 2.56^{+0.71}_{-0.70}$, $\rho_c = 0.67^{+0.69}_{-0.46}$ ($\rho_c^{\rm up} = 3.1$), and $\rho_d = 5.1^{+1.3}_{-1.2}$ g cm^{-3}. We note that the RV-undetected TOI-396 c would be the least dense planet, while the densest planet is the outermost one (i.e. TOI-396 d), which constitutes a quite atypical architecture within the observed exoplanet population (e.g. Ciardi et al. 2013; Weiss et al. 2018; Mishra et al. 2023). However, this conclusion is just tentative, given the uncertainties on the mean planetary densities. Moreover, the detection level of the RV-inferred parameters of TOI-396 c is not statistically significant. We further tested whether including the MINERVA-Australis (Addison et al. 2019) RV data (30 measurements as taken from Vanderburg et al. 2019) can help detect the elusive planet. However, it turned out that their precision level (∼ 6 m s^{-1}) is not high enough to improve the characterisation of the system. In other words, the RV semi-amplitudes we obtained are consistent and indistinguishable within the statistical fluctuation with what was derived from the more precise *HARPS* data set. This led us to further check that TOI-396 c indeed belongs to this system (Sect. 5.2) and to investigate the reason for its RV non-detection (Sect. 5.3).

5.2. Joint LC and RV analysis accounting for TTVs

As planet c is undetected in the RV time series, one may wonder whether TOI-396 c is a false positive. However, by using the VESPA tool (Morton 2012, 2015) that accounts for the constraints from the *TESS* LCs, imaging, and spectroscopy, Vanderburg et al. (2019) already computed that the false-positive probabilities (FPPs) are lower than 10^{-3} for all three planets.

In line with Vanderburg et al. (2019), we also confirmed that the P_c/P_b period ratio is commensurable and differs from the 5:3 ratio by less than 0.027%. As planets with orbits in, or close to,

---

[5] http://kurucz.harvard.edu/grids.html.
[6] https://github.com/nespinoza/limb-darkening

resonances are likely to show TTVs, we decided to repeat the same MCMC analysis outlined above, but enabling the transit timings of each transit event to vary to then compute the TTV amplitude with respect to the linear ephemerides model derived in Sect. 5.1. All jump parameters converged ($\hat{R} \lesssim 1.01$). The medians of the posterior distributions of the most relevant system parameters along with the 68.3% confidence intervals are listed in Table 2. The phase-folded LCs of the three planets are shown in Figure 1, while the phase-folded RV time series are displayed in Figure 2. In particular, the middle panel of Fig. 2 shows that, after subtracting the RV signals of both planets b and d, the RV time series looks flat consistently with the non-detection of TOI-396 c.

This analysis gives $R_b = 2.004^{+0.045}_{-0.047} R_\oplus$, $R_c = 1.979^{+0.054}_{-0.051} R_\oplus$, and $R_d = 2.001^{+0.063}_{-0.064} R_\oplus$ and confirms the RV detection of TOI-396 b and TOI-396 d (at the 3.8 and 4.5σ-level, respectively) with $M_b = 3.55^{+0.94}_{-0.96} M_\oplus$ and $M_d = 7.1 \pm 1.6 M_\oplus$. These outcomes are consistent with the results obtained from the analysis that assumes linear ephemerides (Sect. 5.1).

Fig. 3 shows the three planets of the system (star symbol) along with other exoplanets whose density is more significant than the 3σ level[7] (circular marker) in the mass-radius (MR) diagram. The superimposed theoretical MR models as taken from Aguichine et al. (2021, A21) and Haldemann et al. (2024) help guide the eye; however, we warn the reader of possible degeneracies occurring in the MR plane. A thorough internal structure analysis of the well characterised TOI-396 b and d is presented in Sect. 7.

We found significant TTV signals for planet b and c (see Figure 4, Top and Middle panels) as expected from the commensurability of their periods. The TTV statistical significance of TOI-396 b and c is evident even by eye when comparing the data points location with the shaded regions that represent the 1σ uncertainties of the linear ephemerides. For each planet, we further quantified the reduced-χ^2 ($\hat{\chi}^2$) characterising the TTV amplitudes via

$$\hat{\chi}^2_j = \frac{1}{N_{\mathrm{tr},j} - 2} \sum_{i=1}^{N_{\mathrm{tr},j}} \left(\frac{\mathrm{TTV}_{j,i}}{\sigma_{j,i}} \right)^2 \qquad (1)$$

where $N_{\mathrm{tr},j}$ is the number of transit event of the j-th planet. We obtained $\hat{\chi}^2_b = 4.4$, $\hat{\chi}^2_c = 4.1$, and $\hat{\chi}^2_d = 0.7$ for planets b, c, and d, respectively, which confirms the significance of the TTV amplitudes for TOI-396 b and c.

Furthermore, the TTV amplitudes of TOI-396 b and c exhibit a clear anti-correlation pattern that we highlight by superimposing the TTV measurements in Figure A.1. This is a typical signature of gravitational interaction between the two planets, which confirms that TOI-396 c belongs to the system despite its elusiveness in the RV time series. For each planet, the timing of each transit event and the corresponding TTV amplitude computed with respect to the linear ephemerides are listed in Table A.3.

5.3. Discussion regarding why TOI-396 c is not detected in the RV time series

Magnetic activity combined with stellar rotation induces RV variations that can hide, affect, or even mimic planetary signals (e.g. Queloz et al. 2001; Hatzes et al. 2010; Dumusque et al.

---

[7] The planet properties were downloaded from the Nasa Exoplanet Archive as of 5 June 2024: https://exoplanetarchive.ipac.caltech.edu/

Fig. 1: *TESS* detrended and phase-folded LCs (blue dots) of TOI-396 b (*Top panel*), TOI-396 c (*Middle panel*), and TOI-396 d (*Bottom panel*) with the transit model superimposed in red. The black markers are the binned data points (binning 20 min).

2011a; Haywood et al. 2014; Suárez Mascareño et al. 2017; Gandolfi et al. 2017). A possible explanation for the non-detection of the Doppler reflex motion induced by TOI-396 c is that stellar activity destructively interferes with the Keplerian signal of the planet. This may happen if the star has a rotation period

Table 2: System parameters as derived from the joint LC and RV analysis accounting for TTVs.

Parameter	Symbol	TOI-396 b	TOI-396 c [c]	TOI-396 d
Orbital period	$P^{(a)}$ [d]	$3.585287^{+0.000009}_{-0.000012}$	$5.973865^{+0.000015}_{-0.000016}$	$11.230511^{+0.000043}_{-0.000045}$
Transit timing	$T_0^{(a)}$ [BJD]	$8409.1900^{+0.0011}_{-0.0012}$	$8415.63344^{+0.00099}_{-0.00093}$	$8409.7324^{+0.0028}_{-0.0025}$
Transit depth	dF [ppm]	$213.7^{+6.5}_{-6.4}$	$208.7^{+8.5}_{-8.3}$	213^{+12}_{-11}
Impact parameter	b	$0.587^{+0.025}_{-0.028}$	$0.701^{+0.017}_{-0.019}$	$0.712^{+0.026}_{-0.023}$
RV semi-amplitude	K [m s^{-1}]	$1.30^{+0.34}_{-0.35}$	$0.28^{+0.29}_{-0.19}$	1.78 ± 0.40
Transit duration	W [h]	$2.705^{+0.038}_{-0.034}$	$2.843^{+0.046}_{-0.043}$	$3.47^{+0.08}_{-0.13}$
Semi-major axis	a [AU]	0.04888 ± 0.00066	0.06870 ± 0.00092	0.1046 ± 0.0014
Orbital inclination	i [°]	$85.98^{+0.26}_{-0.25}$	$86.59^{+0.15}_{-0.14}$	$87.72^{+0.10}_{-0.11}$
Scaled semi-major axis	$a/R_\star$	$8.37^{+0.17}_{-0.16}$	$11.77^{+0.24}_{-0.22}$	$17.93^{+0.37}_{-0.34}$
Equilibrium temperature	$T_{\rm eq}^{(b)}$ [K]	1552^{+22}_{-23}	1309 ± 19	1061^{+15}_{-16}
Eccentricity	e	0 (fixed)	0 (fixed)	0 (fixed)
Argument of pericentre	ω [°]	90 (fixed)	90 (fixed)	90 (fixed)
Planet radius	R_p [$R_\oplus$]	$2.004^{+0.045}_{-0.047}$	$1.979^{+0.054}_{-0.051}$	$2.001^{+0.063}_{-0.064}$
Planet mass	M_p [$M_\oplus$]	$3.55^{+0.94}_{-0.96}$	$0.90^{+0.94}_{-0.63}$	7.1 ± 1.6
Planet density	ρ_p [g cm^{-3}]	$2.44^{+0.69}_{-0.68}$	$0.65^{+0.67}_{-0.45}$	$4.9^{+1.2}_{-1.1}$
LD coefficient 1	$u_{1,\rm TESS}$	$0.2318^{+0.0066}_{-0.0064}$		
LD coefficient 2	$u_{2,\rm TESS}$	$0.3084^{+0.0030}_{-0.0029}$		
RV jitter	σ_{HARPS} [m s^{-1}]	$1.490^{+0.041}_{-0.022}$		

Notes. All jump parameters, but the LD coefficients, were subject to unbounded uniform priors following the parameterisations specified in Bonfanti & Gillon (2020); see text for further details. [a] Uncertainties from the run assuming linear ephemerides (no TTVs). T_0 values are shifted by $-2\,450\,000$. [b] Assuming zero albedo and full recirculation. [c] The 3σ upper limits on the RV semi-amplitude, the planet mass, and the mean planet density of TOI-396 c are $K_c^{\rm up} = 1.2$ m s^{-1}, $M_c^{\rm up} = 3.8\ M_\oplus$, and $\rho_c^{\rm up} = 2.9$ g cm^{-3}, respectively.

comparable to the orbital period of the planet (e.g. Vanderburg et al. 2016). Disentangling the planetary signal from stellar activity and retrieving the Doppler motion induced by the orbiting planet would then be challenging (e.g. Dragomir et al. 2012; Kossakowski et al. 2022).

In order to investigate this hypothesis, we performed a frequency analysis of the line profile variation diagnostics (FWHM, contrast, and skewness) and activity indicators (log R$'_{\rm HK}$ and Hα indexes). Figure 5 displays the time series (left column), along with the respective generalised Lomb-Scargle (GLS, Zechmeister & Kürster 2009) periodograms (right column). We assessed the significance of the peaks detected in the power spectra by estimating their false alarm probability (FAP), that is the probability that noise could produce a peak with power higher than the one we found in the time series. To account for the possible presence of non-Gaussian noise in the data, we estimated the FAP using the bootstrap randomisation method (see, e.g., Murdoch et al. 1993; Kuerster et al. 1997; Hatzes 2019). Briefly, we computed the GLS periodogram of 10^5 mock time series obtained by randomly shuffling the data points along with their error bars, while keeping the timestamps fixed. We defined the FAP as the fraction of those mock periodograms whose highest power exceeds the power of the real data at any frequency. In the present work, we considered a peak to be significant if its false alarm probability is FAP < 0.1 %.

We found that the time series of the log R$'_{\rm HK}$ and Hα indexes display long-term trends likely due to the magnetic cycles of the star (Fig. 5, left column, first and third panels). In the Fourier domain, these trends translate into a significant (FAP < 0.1 %) excess of power at frequencies lower than the spectral resolution[8] of our HARPS observations (Fig. 5, right column, first and third panels). We modelled these long-term signals as quadratic trends and subtracted the best-fitting parabolas from the respective time-series. The GLS periodograms of the residuals of the activity indicators display significant peaks between ~6 and 8 d (i.e, between ~0.0125 and 0.167 d^{-1}; Fig. 5, yellow area). The peaks are equally spaced by ~0.0068 d^{-1}, which coincides with a peak found in the periodogram of the window function. Given the current data at our disposal, we are not able to distinguish between true frequencies and aliases. Although not significant, the power spectra of the contrast and skewness show peaks in the same frequency range, suggesting that the rotation period of the star might be ~6–8 d.

We note that the periodogram of the FWHM also displays an excess of power at low frequencies. However, the corresponding peak remains below our 0.1 %-FAP significance threshold (see Fig. 5, second to last panel). Yet, if we apply the same procedure

---

[8] The spectral resolution is defined as the inverse of the time baseline. Our observations cover a baseline of about 177.4 d, which yields a spectral resolution of ~0.0056 d^{-1}.
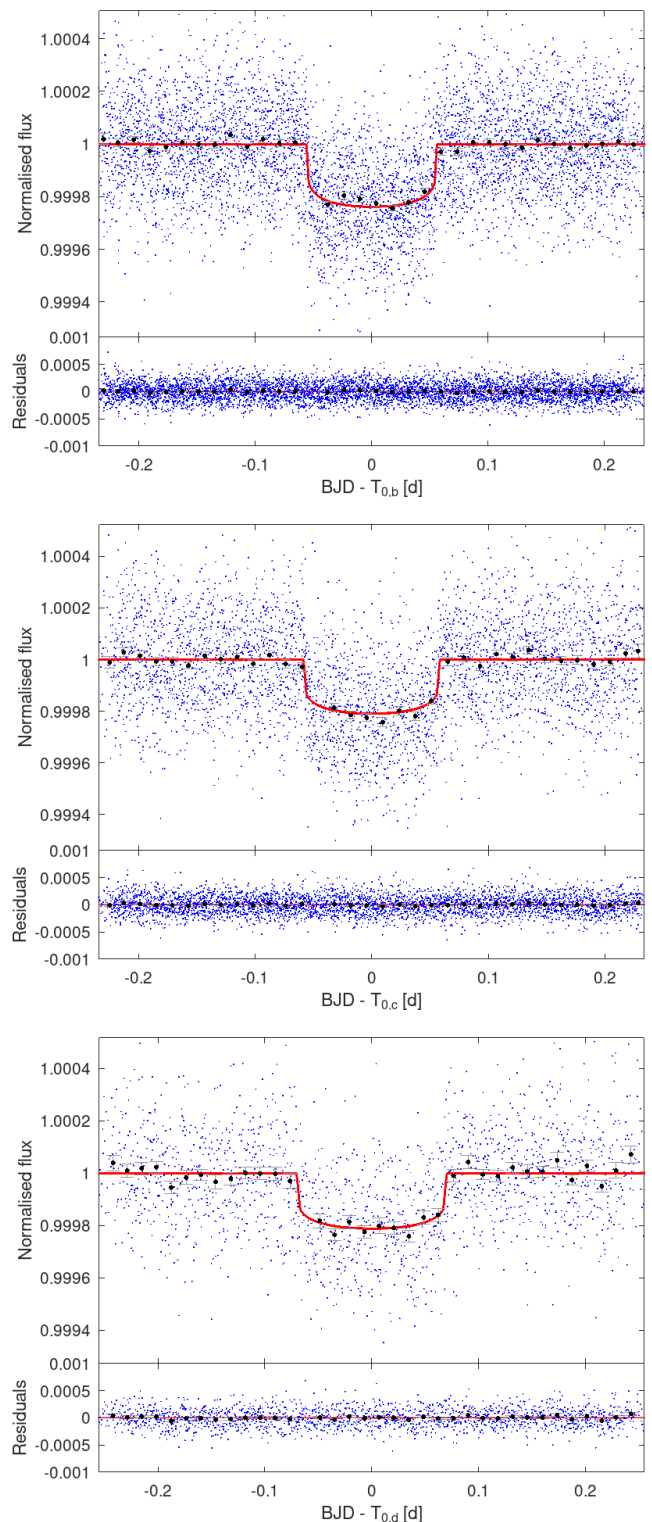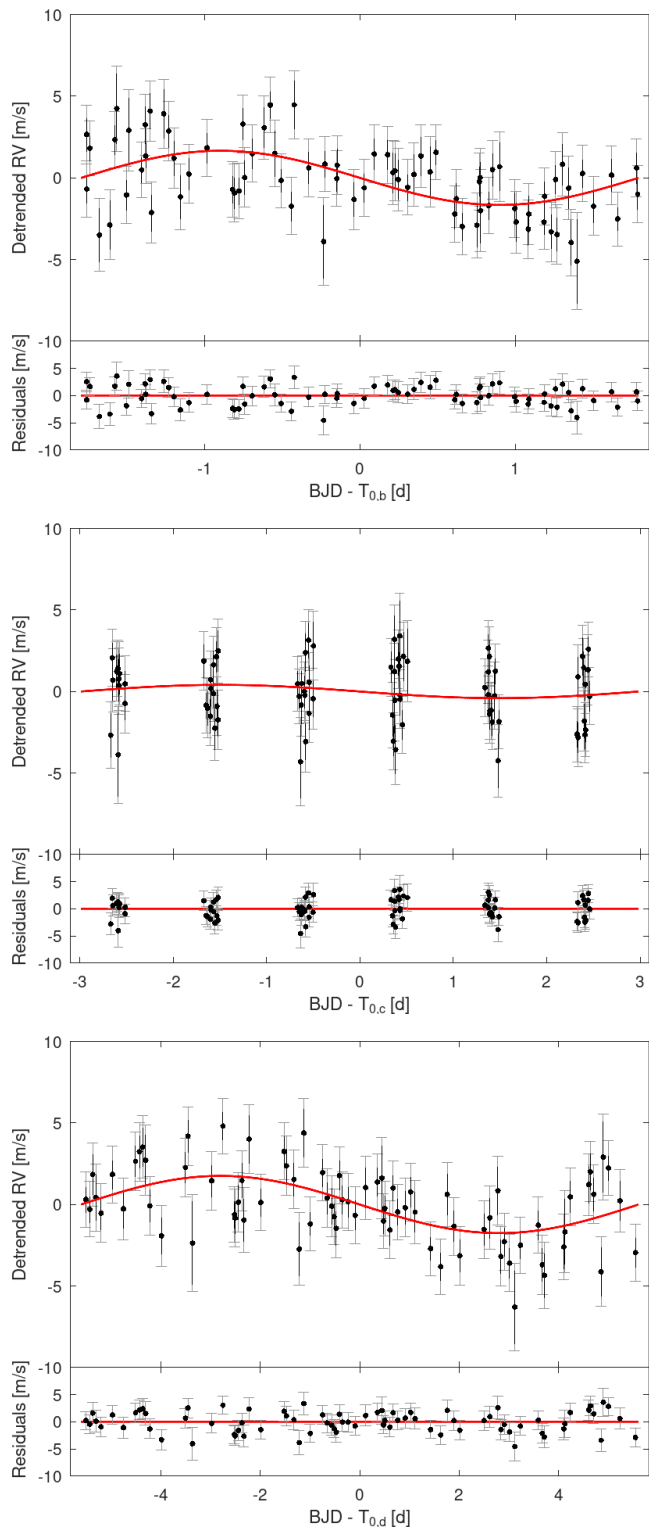
Fig. 2: *HARPS* detrended and phase-folded RV time series of TOI-396 b (*Top panel*), TOI-396 c (*Middle panel*), and TOI-396 d (*Bottom panel*) with the Keplerian model superimposed in red. For each planet, the time series were obtained after subtracting the RV contribution of the other planets. The error bars also account for the jitter contribution (displayed in grey).
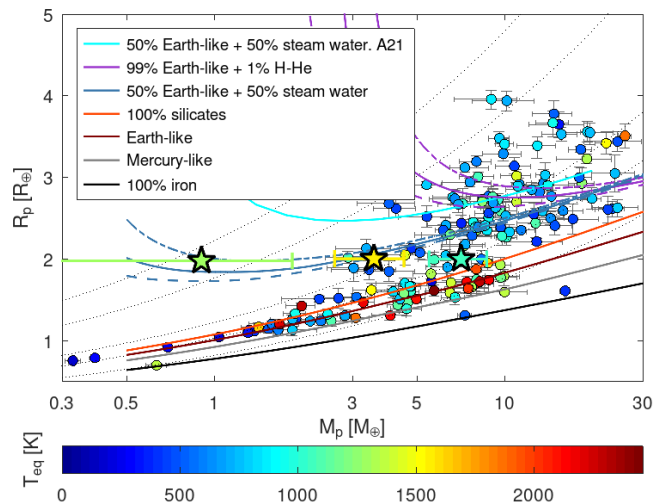
Fig. 3: Mass-radius diagram showing the three planets orbiting TOI-396 (star symbol) along with the exoplanets whose density is more significant than the 3σ level (circle). All the markers are colour-coded according to the equilibrium temperature ($T_{\rm eq}$) of the planets. The thick lines are the theoretical MR BICEPS models as detailed in the legend, except for the light-blue line denoted with A21, which is taken from Aguichine et al. (2021). Earth-like means 32.5% iron + 67.5% silicates, while Mercury-like means 70% iron + 30% silicates. Models were computed for $T_{\rm eq} = T_{{\rm eq},b} = 1552$ K (dashed-dotted lines), $T_{\rm eq} = T_{{\rm eq},c} = 1309$ K (solid lines), and $T_{\rm eq} = T_{{\rm eq},d} = 1061$ K (dashed lines). The difference between the A21 model and its BICEPS counterpart is due to different assumptions for e.g. pressure-temperature profiles and opacities. The dotted black lines are the iso-density loci of points corresponding to 0.5, 1, 3, 5, 10 g cm^{-3} (going from top to bottom). We recall that the mass estimate of TOI-396 c (the leftmost star symbol) is not statistically significant and its 3σ upper limit is $M_c^{\rm up} \sim 4\,M_\oplus$.

The projected equatorial velocity of the star ($v \sin i_\star = 7.5 \pm 0.2\,{\rm km\,s^{-1}}$), along with its radius ($R_\star = 1.258 \pm 0.019\,R_\odot$), yields an upper limit for the rotation period of $P_{\rm rot}^{\rm up} = 8.5 \pm 0.3$ d. Using the mean value[9] of $\log R'_{\rm HK} = -4.926 \pm 0.014$, we inferred a stellar rotation period of 6.7 ± 1.3 d and 6.9 ± 1.3 d from the empirical equations of Noyes et al. (1984) and Mamajek & Hillenbrand (2008), respectively. In addition, by inputting the isochronal age into the gyrochronological relation from Barnes (2010), we computed a stellar rotation period of $7.1^{+1.0}_{-1.1}$ d. These results corroborate our interpretations that the peaks between 6 and 8 d significantly detected in the power spectra of the activity indicators originate from stellar rotation.

To check whether a quasi-periodic signal compatible with ~ 7 d is also present in the photometric data, for each *TESS* sector we extracted custom LCs from pixel data using `lightkurve` (Lightkurve Collaboration et al. 2018). In detail, we adopted the default quality bitmask and set the aperture to 'all', which corresponds to an aperture larger than the one used by the official SAP pipeline. In fact, larger apertures mitigate the effect of slow image drifts that could interfere with slow flux changes, such

described above and remove this signal by fitting a quadratic trend to the FWHM time series, we find no significant peak in the residuals.

---

[9] Rather than assigning to the mean an uncertainty equal to the standard error, we adopted a more conservative uncertainty equal to the standard deviation of our 78 measurements.
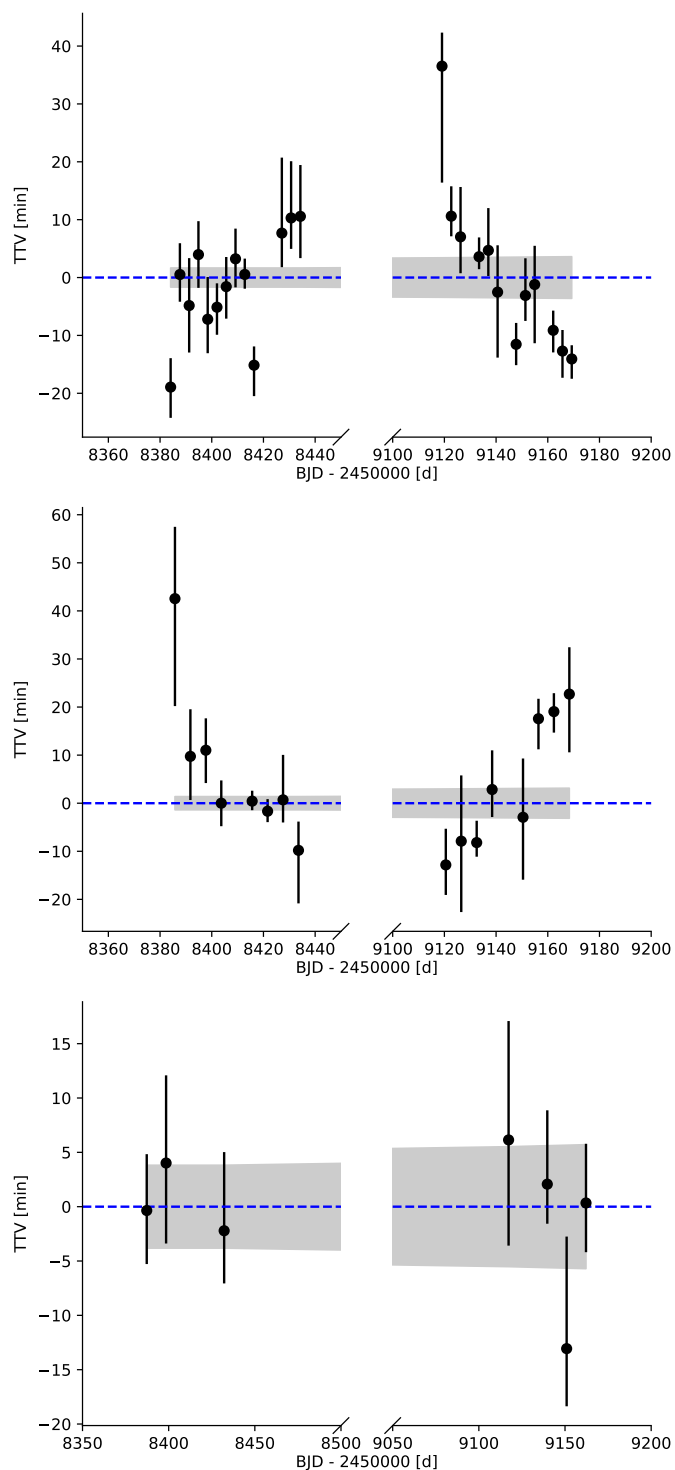
Fig. 4: TTV amplitudes obtained for TOI-396 b (*Top panel*), TOI-396 c (*Middle panel*), and TOI-396 d (*Bottom panel*). The grey shaded region highlights the 1σ uncertainty region as derived from error propagation of the linear ephemerides.

as the 6–8 d rotation period signals we aim to detect. After removing the temporal windows containing the transit events, we computed the GLS periodograms of these `lightkurve`-based LCs. The FAP was computed following the same bootstrap technique outlined above for the RV activity indicators. The four periodograms (Fig. A.2, first column) exhibit very significant peaks at ~ 7.7, 7.9, 7.5, and 6.8 days for *TESS* Sectors 3, 4, 30, and 31,

Table 3: Radial velocity semi-amplitudes K_{out} as retrieved from MCMCI analyses of the RV time series obtained by adding an artificial Keplerian signal with period $P = P_c$ and semi-amplitudes K_{in} to the original *HARPS* time series.

K_{in} [m s^{-1}]	ρ_p [g cm^{-3}]	M_p [$M_\oplus$]	K_{out} [m s^{-1}]	Detection level
0.51	1.0	1.6	0.68 ± 0.36	$\sim 2\sigma$
0.77	1.5	2.3	0.93 ± 0.42	$\sim 2\sigma$
1.0	1.9	3.0	1.15 ± 0.38	$\sim 3\sigma$
$K_d = 1.79$	3.5	5.4	1.94 ± 0.38	$\sim 5\sigma$

Notes. Columns ρ_p and M_p translate the injected synthetic signals into the corresponding physical parameters of the planet, while the last column quantifies the K_{out} detection level in terms of σ.

respectively. Except for Sector 30, they are not the most prominent peaks; however, they persist even after removing the most significant signals (Fig. A.2, second column). Whereas we acknowledge that the likely rotation period of the star is close to the first harmonic of the orbital period of *TESS* around the Earth ($P_{rot,\star} \sim \frac{1}{2} P_{TESS} \sim 14$ days), the photometric signal at 6–8 d is significant in all the four *TESS* sectors and persists after prewhitening the data. This signal is consistent with the rotation period detected in the HARPS activity indicators and inferred from $\log R'_{HK}$, $v \sin i_\star$, and gyrochronology, suggesting it is astrophysical in nature and due to the presence of active regions carried around by stellar rotation. Assuming the $\log R'_{HK}$-based $P_{rot,\star} = 6.7 \pm 1.3$ d as our reference estimate, the orbital period of TOI-396 c ($P_c \sim 6$ d) is close to $P_{rot,\star}$, which may explain the non-detection of planet c within the RV time series.

If some kind of destructive interference between the Keplerian signal of planet c and the stellar activity has occurred, any artificial Keplerian signals with period $P = P_c$ added to the observed RV time series should in principle be retrieved. To test this hypothesis, we considered Keplerian signals of the following form

$$RV_{art} = -K_{art} \sin\left[\frac{2\pi}{P}(t - T_0)\right] \qquad (2)$$

and generated four different RV time series by separately adding to the *HARPS* time series synthetic RV signals following Equation (2) with $P = P_c$, $T_0 = T_{0,c}$, and $K_{art} = K_{in}$, where K_{in} are the four different amplitude values listed in the first column of Table 3. For each RV time series, we then performed an MCMCI analysis to retrieve the RV semi-amplitude of the artificial signal (K_{out}; see Table 3).

We note that the resulting $K_{out} \approx K_{in} + K_c$, where $K_c = 0.28^{+0.29}_{-0.19}$ m s^{-1} is the RV semi-amplitude of planet c as derived from the analysis on the original RV time series. As we essentially retrieved what we inserted in the *HARPS* time series, we may conclude that the destructive interference between the RV signals induced by the star and by planet c has already occurred and any further RV signal added to the RV time series is detected.

As $P_{rot,\star}$ is not exactly equal to P_c, we then repeated the test outlined above, but this time we injected into the original *HARPS* time series artificial Keplerian signals with $P = P_{rot,\star}$. The K_{out} values obtained by the MCMC analyses depending on the different K_{in} values are reported in Table 4. The K_{out} values are systematically and significantly smaller than the corresponding K_{in} values, which a posteriori supports the conclusion that the stellar rotation period is around 6–8 d. Furthermore, a planet with this
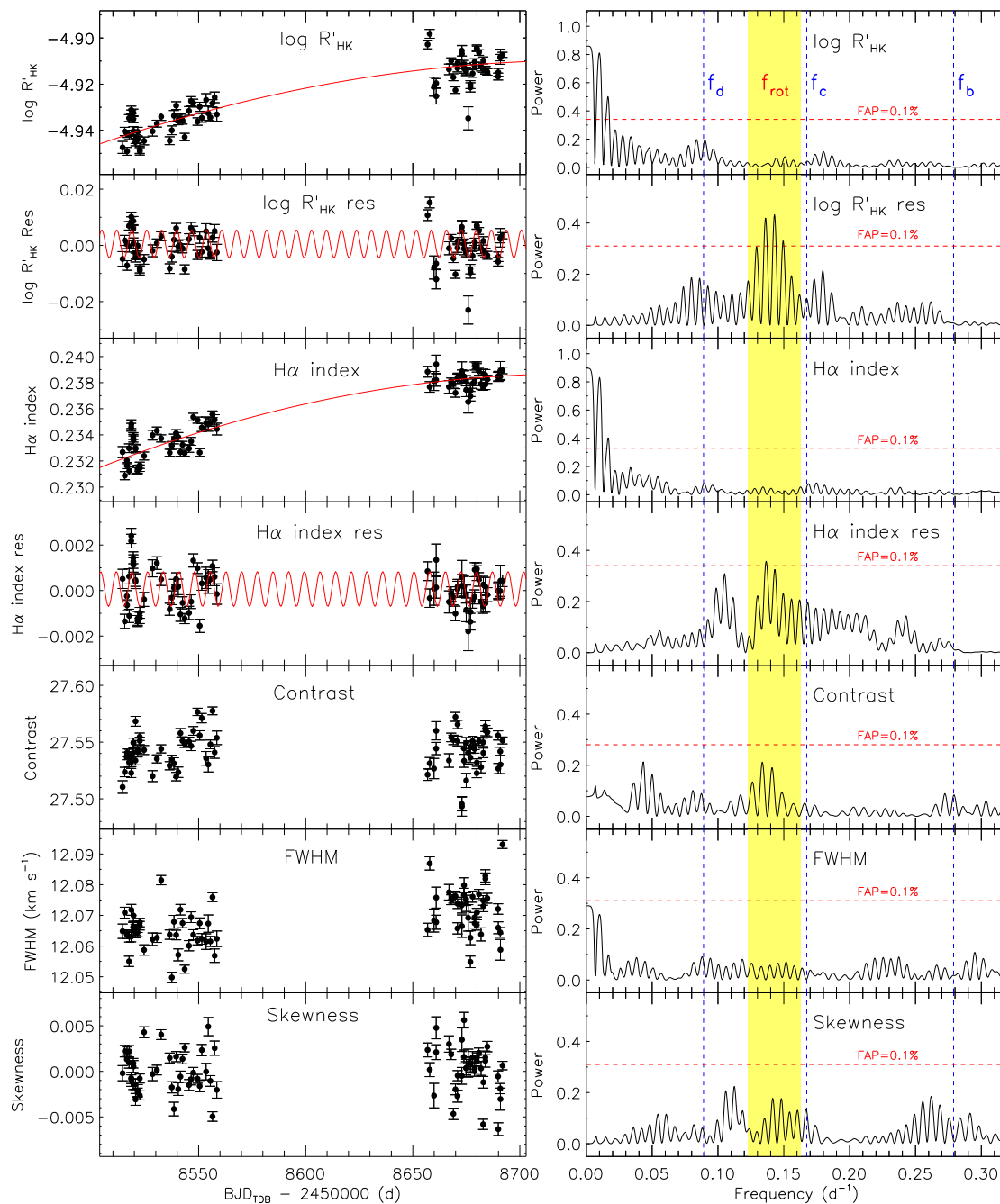
Fig. 5: Time series (left panels) and GLS periodograms (right panels) of the line profile variation diagnostics and activity indicators extracted from TOI-396's HARPS spectra. In the left panels, the red curves in the first four panels mark the quadratic trends and sine functions as obtained from the best fit to the most significant peaks (false alarm probability FAP < 0.1%) identified in the corresponding GLS periodograms. In the right panels, the vertical dashed blue lines mark the orbital frequencies of the tree transiting planets. The yellow area encompasses the peaks likely due to stellar rotation. The horizontal dashed red lines mark the 0.1% false alarm probability.

orbital period would be firmly detected if its RV semi-amplitude were greater than K_d, which is the largest RV semi-amplitude detected for this system. Instead, by injecting a Keplerian signal with $K_{in} = K_d$ and $P = P_{rot,\star}$, the MCMCI analysis is able to barely detect (at ~2σ) a planetary signal whose amplitude is half of that expected. The detection level increases when K_{in} increases; however, we still underestimate K_{out}. These tests prove that it is difficult to retrieve planetary signals with $P \sim P_{rot,\star}$.

In summary, we conclude that stellar activity is responsible for generating spurious RV signals whose harmonics also include the stellar rotation period. As a consequence, it is hard to reliably detect planets with orbital periods comparable to $P_{rot,\star}$ via the RV technique and Table 4 quantifies the magnitude of this effect. We note that the K_c we obtained from the MCMCI analysis in Sect. 5.2 is comparable to the K_{out} retrieved when inserting an artificial signal having $K_{in} = 1.0$ m s^{-1}, which let us

Table 4: Same as Table 3, but this time the Keplerian signals with $K = K_{in}$ have period $P = P_{rot,\star}$.

K_{in} [m s^{-1}]	ρ_p [g cm^{-3}]	M_p [$M_\oplus$]	K_{out} [m s^{-1}]	Detection level	$\frac{\Delta K}{K}$	ΔK [σ]
1.0	2.0	3.1	0.29 ± 0.28	~ 1σ	−71%	−2.5
K_d = 1.79	3.6	5.6	0.80 ± 0.39	~ 2σ	−55%	−2.5
3.0	6.1	9.4	1.90 ± 0.40	~ 5σ	−37%	−2.8
10.0	20.2	31.4	9.02 ± 0.36	~ 25σ	−10%	−2.7

Notes. Column $\frac{\Delta K}{K}$ gives the relative difference (in percentage) between the obtained RV semi-amplitude (K_{out}) and the expected one (K_{in}), while the last column $\Delta K \equiv K_{out} - K_{in}$ lists the semi-amplitude difference in terms of the 1σ uncertainty of K_{out}.

to speculate that TOI-396 c might have $M_c \sim 3.0 \, M_\oplus$ and $\rho_c \sim 2.0$ g cm^{-3}.

6. Joint RV and TTV dynamical analysis

As mentioned, the anti-correlation pattern of the observed TTVs (see Fig. A.1) is a typical signal of the dynamical interaction between TOI-396 b and c. However, the data in our hands are not enough to currently derive meaningful planetary masses from the TTVs. Indeed, the photometric observations are clustered in two groups (about two years apart), which results in a partial coverage of the curvature of the TTVs. This prevents us from accurately mapping the full phases and super-periods of the TTV signals. Hence a dynamical fit onto the transit times would lead to a high fraction of low-amplitude TTVs with a short super-period or to a low fraction of high-amplitude long-period TTV signals.

Despite this, we attempted to run a dynamical joint fit of the TTV and RV data set with TRADES[10] (Borsato et al. 2014, 2019, 2021), a Fortran-python code developed to model TTVs and RVs simultaneously along with N-body integration. We have taken and fixed the stellar mass and radius values from Table 1. We further fixed the orbital inclinations i to the values in Table 2 and the longitude of the ascending nodes to $\Omega = 180°$[11] for all the planets. We fitted the planetary masses scaled by the stellar mass ($M_{b,c,d}/M_\star$), the orbital periods (P), the eccentricities (e) and the arguments of the pericentre (ω) in the form ($\sqrt{e}\cos\omega$, $\sqrt{e}\sin\omega$), and the mean longitudes (λ[12]). We also fitted for an RV offset (γ_{RV}) and for an RV jitter term (σ_{jitter}) by adopting $\log_2 \sigma_{jitter}$ as step parameter, although we used the de-trended RV data set as derived from Sect. 5.2, where a jitter term was already included in the RV errors. All fitting parameters were subject to uniform priors that account for their respective physical boundaries (see Table 5); for the eccentricities we applied a log-penalty ($\log p_e$) based on the half-Gaussian ($e = 0, \sigma_e = 0.083$) from Van Eylen et al. (2019).

The reference time for the dynamical integration of the orbital parameters was set at $T_{ref} = 2\,458\,379$ BJD$_{TDB}$, that is before all available observations. We combined the quasi-global differential evolution (Storn & Price 1997) optimisation algorithm implemented in PyDE (Parviainen et al. 2016)

with the Affine Invariant MCMC Ensemble sampler (Goodman & Weare 2010) EMCEE implemented by Foreman-Mackey et al. (2019, 2013). We first ran PyDE and evolved 68 different initial configurations of parameter sets for 50 000 generations (number of steps for which each parameter is evolved). To perform the dynamical analysis in an MCMC fashion, we then ran EMCEE, assuming as starting point the outcome obtained with PyDE. We set up 68 chains for 600 000 steps each. To sample the parameter space efficiently, we mixed the DEMove() and DESnookerMove() differential evolution moves[13] in the proportion 80%–20% (Nelson et al. 2014; ter Braak & Vrugt 2008). We repeated the sequence PyDE+EMCEE twice, with different seeds for the random number generator. The chains reached convergence according to visual inspection and statistical indicators, such as the Gelman-Rubin $\hat{R}$, the Geweke's statistic (Geweke 1991), and the auto-correlation function[14]. For both runs, we applied a conservative thinning factor of 100 and discarded the first 50% of the chains (burn-in). For each run, we derived the reference outcome (hereinafter also referred to as best-fit), as the maximum-a-posteriori (MAP) parameters' set, that is the set of parameters that maximises the log-probability[15]. The uncertainty of each parameter is quantified by the high-density interval (HDI) at 68.27%[16] of its posterior distribution. For each parameter we computed a Z-score defined as Z-score = |MAP$_1$ − MAP$_2$|/ $\sqrt{\max|\text{ERR}_1|^2 + \max|\text{ERR}_2|^2}$, where the subscripts denote the two different runs and ERR = HDI − MAP. It turned out that Z-score < 1 for each parameter, which allows us to merge the posterior distributions deriving from the two runs to finally compute the MAP and the respective HDI from the merged posterior distributions. We further checked the Hill stability of the system (Sundman 1913) when assuming the entire merged posterior distributions by calculating the angular momentum deficit (AMD, Laskar 1997, 2000; Laskar & Petit 2017) criterion (Eq. 26 from Petit et al. 2018). Table 5 lists the parameters returned by TRADES (MAP and HDI) along with their respective priors.

We note that the dynamical integration with TRADES allowed for a significant detection (>3σ) of the mass of TOI-396 c, that is $M_{c,dyn} = 2.24^{+0.13}_{-0.67} \, M_\oplus$. However, as explained above, *TESS* data do not allow us to fully map the TTV pattern. Therefore, the present-day estimate of $M_{c,dyn}$ only provides an indication of the possible mass of the planet that might not be accurate, despite its formal precision. Indeed, to accurately and reliably determine planetary masses via TTVs, it is necessary to monitor the TTV signal by benefiting of a full sampling coverage, as demonstrated for example by the cases of Kepler-9 (Holman et al. 2010) and K2-24 (Petigura et al. 2016), whose orbital parameters and masses were comprehensively revisited by Borsato et al. (2014) and Petigura et al. (2018); Nascimbeni et al. (2024), respectively. In detail, Holman et al. (2010) had reported the masses of Kepler-9 b and c with a precision better than 8%, by performing a TTV analysis on the first three quarters of the Kepler data. Later on, by benefiting of twelve sectors of Kepler data that enabled the full mapping of the TTV phase, Borsato et al. (2014) obtained TTV-based masses differing by a

---

[10] https://github.com/lucaborsato/trades

[11] We assumed the same reference system of Winn (2010) and Borsato et al. (2014) and later used in Borsato et al. (2019, 2021, 2024); Nascimbeni et al. (2023, 2024).

[12] The mean longitude is defined as $\lambda = \omega + \Omega + \mathcal{M}$, where ω is the argument of the pericentre, Ω is the longitude of the ascending node, and $\mathcal{M}$ is the mean anomaly.

[13] See EMCEE documentation: https://emcee.readthedocs.io/en/stable/tutorials/moves/

[14] See e.g. Goodman & Weare (2010) and the EMCEE documentation at https://emcee.readthedocs.io/en/stable/tutorials/autocorr/#autocorr

[15] The log-probability is given by $\log \mathcal{P} = \log \mathcal{L} + \log p_e$, where $\log \mathcal{L}$ is the log-likelihood and $\log p_e$ is the log-penalty of the eccentricities.

[16] An HDI at 68.27% is the equivalent of the 15.87th − 84.14th percentile range of a Normal distribution that provides the 1σ standard confidence interval.

factor ~ 2 from the estimate of Holman et al. (2010). Similarly, by accounting on more photometric data, Petigura et al. (2018); Nascimbeni et al. (2024) found that the mass of K2-24 c is lower by almost 2σ than the estimate of Petigura et al. (2016) who had claimed a detection at the $\sim 4\sigma$ level.

After extracting all the synthetic transit timings T_{tr} (i.e. the 'observed': O) from TRADES' analysis, we computed the 'calculated' (C) counterpart according to the linear ephemerides model based on what listed in Table 2. We plotted the $O - C$ as a function of time as well as the RV best-fit model in Figures 6 and 7.

Additionally, we investigated if the best-fit configuration is in or close to an MMR. We integrated the MAP parameters with the N-body code rebound (Rein & Liu 2012) and the symplectic Wisdom-Holman integrator whfast (Rein & Tamayo 2015; Wisdom & Holman 1991) for $10\,000$ years. We computed the evolution of the critical resonance angles of TOI-396 b and TOI-396 c

$$\phi_b = p\lambda_b - (p + q)\lambda_c + q\varpi_b$$
$$\phi_c = p\lambda_b - (p + q)\lambda_c + q\varpi_c, \qquad (3)$$

where $p = 3$ and $q = 2$ (for a second order 5:3 MMR), while $\varpi \equiv \omega + \Omega$ is the longitude of the pericentre. We also computed the evolution of $\Delta\varpi \equiv \varpi_b - \varpi_c = (\phi_b - \phi_c)/q$. In case of MMR, we expect that both ϕ_b and ϕ_c librate (i.e. oscillate) around a fixed value for the entire orbital integration. Instead, if these angles circulate, that is they span the full $0°–360°$ range (or equivalently the $-180°–180°$ range), then the planet pair is not in resonance. We found that both ϕ_b and ϕ_c circulate (see the two upper panels of Fig. 8), which indicates that the system is not in an exact 5:3 MMR. Even if $\Delta\varpi$ seems to oscillate around $0°$, it circulates every $\sim 2\,000$ years (bottom panel of Fig. 8), which further confirms that the system is not trapped in an MMR state. We also found the same behaviour for the resonant angles of 200 random samples drawn from the posterior distribution (not shown here). Our conclusions are consistent with the simulations performed by Vanderburg et al. (2019), who found that most realisations of the system are not in resonance.

As shown in Fig. 6, the MAP parameter set predicts that the TTV super-period is longer than the time spanning the two clustered TESS observations. We decided to track the potential evolution of the TTV signals over a temporal baseline of ~ 5.2 years. To this end, we ran forward numerical N-body simulations with TRADES, setting the initial conditions of the orbital parameters to be integrated at $t = T_{ref}$. We ran a first simulation taking all the parameters from the MAP solution. Then, we further ran 200 simulations, where the sets of the system's parameters were randomly drawn from the merged posterior distributions. We computed the synthetic (i.e. observed: O) transit times T_{tr} and created a simulated $O - C$ plot against time, where the C counterpart of T_{tr} was computed assuming the linear ephemerides of Table 2. The results are displayed in Fig. 9 that emphasises a progressive drift of the $O - C$ values inferred from the MAP parameters (black line) with respect to the zero value. As a consequence, the TTV amplitudes of planets b and c increase with time. In particular, the semi-amplitude of the $O - C$ black curves are about two and five hours for b and c, respectively. The TTV super-period seems to be roughly equal to or larger than the integration time span, that is ~ 5 years. The variance of the TTV amplitude (shaded area) is inferred from the results of the additional 200 simulations and reflects the widths of the posterior distributions from which the system's parameters were drawn. The remarkable $O - C$ drifts (i.e. the poorly constrained linear

ephemerides) combined with the uncertainty on the TTV amplitudes make challenging to plan future observations of planets b and c, as the actual transit timings might differ from the linear ephemerides predictions by ~ 5 and ~ 10 hours for TOI-396 b and TOI-396 c, respectively. *TESS* will not observe the target in the foreseeable future.[17]

7. Internal structure

Using the masses and transit depths reported in Table 2, we ran the neural network based internal structure modelling framework `plaNETic`[18] (Egger et al. 2024) to infer the internal structure of TOI-396 b and d. `plaNETic` uses a full grid accept-reject sampling method in combination with a deep neural network (DNN) that was trained on the forward model of BICEPS (Haldemann et al. 2024) to infer the internal structure of observed planets. Each planet is modelled as a three-layered structure: an inner iron-dominated core, a silicate mantle and a fully mixed envelope made up of water and H/He. In the case of multi-planet systems, all planets are modelled simultaneously.

As modelling the internal structure of exoplanets is a highly degenerate problem, the resulting inferred structure is, at least to a certain extent, dependent on the chosen priors. To mitigate this effect, we ran a total of six models assuming six different combinations of priors. Most importantly, we use two different priors for the water content of the modelled planet, one motivated by a formation scenario outside the iceline (case A, water-rich) and one compatible with a formation inside the iceline (case B, water-poor). For both of these water priors, we choose three different options for the planetary Si/Mg/Fe ratios. In a first case, we assume that these match the stellar Si/Mg/Fe ratios exactly Thiabaud et al. (2015). Second, we assume that the planet is enriched in iron compared to its host star by using the fit of Adibekyan et al. (2021). For option 3, we model the planet independent of the stellar Si/Mg/Fe ratios, but just sampling the planetary ratios uniformly from the simplex where the molar Si, Mg and Fe ratios add up to 1, with an upper bound of 0.75 for Fe. These priors are described in more detail in Egger et al. (2024).

Figures 10 and 11 show the resulting posteriors of the most important interior structure parameters for TOI-396 b and d, respectively, in comparison with the chosen priors (dotted lines). Tables A.4 and A.5 in the Appendix summarise the median and one sigma error intervals for the full set of internal structure parameters. For both planets, the posterior distributions for the core and mantle mass fractions largely agree with the chosen priors for each of the six models that we ran. Indeed, the only planetary structure parameters for which the observational data contributed to their characterisation were the envelope mass fractions. If we assume that the planets formed outside the iceline, we find envelope mass fractions of $28 \pm 10\%$ (A1), $32^{+9}_{-11}\%$ (A2) and $30^{+11}_{-13}\%$ (A3) for planet b and $23^{+12}_{-10}\%$ (A1), $28 \pm 11\%$ (A2) and $26^{+12}_{-13}\%$ (A3) for planet d, with water mass fractions in the envelope of almost 100%. Conversely, if the planets were to have formed inside the iceline, we infer envelope mass fractions of the order of 10^{-5} for planet b and 10^{-4} for planet d, almost entirely made up of H/He.

Table 5: Best-fit parameters (MAP and HDI at 68.27%) along with their respective priors as inferred from the dynamical joint modelling of RVs and TTVs with TRADES.

	TOI-396 b		TOI-396 c		TOI-396 d	
	MAP (HDI)	Prior	MAP (HDI)	Prior	MAP (HDI)	Prior
$M_{\mathrm{p}}/M_\star$ [10^{-6}]	$8.62^{+0.76}_{-2.26}$	$\mathcal{U}(0.02, 52.0)$	$5.59^{+0.25}_{-1.69}$	$\mathcal{U}(0.02, 52.0)$	17^{+3}_{-1}	$\mathcal{U}(0.02, 52.0)$
P [d]	$3.585535^{+0.000092}_{-0.000171}$	$\mathcal{U}(3, 4)$	$5.97291^{+0.00058}_{-0.00031}$	$\mathcal{U}(5, 7)$	$11.230355^{+0.000173}_{-0.000016}$	$\mathcal{U}(10, 12)$
$\sqrt{e}\cos\omega$	$-0.099^{+0.155}_{-0.014}$	$\mathcal{U}(-\sqrt{0.5}, \sqrt{0.5})$	$-0.264^{+0.060}_{-0.017}$	$\mathcal{U}(-\sqrt{0.5}, \sqrt{0.5})$	$-0.168^{+0.069}_{-0.035}$	$\mathcal{U}(-\sqrt{0.5}, \sqrt{0.5})$
$\sqrt{e}\sin\omega$	$-0.268^{+0.038}_{-0.031}$	$\mathcal{U}(-\sqrt{0.5}, \sqrt{0.5})$	$-0.066^{+0.062}_{-0.042}$	$\mathcal{U}(-\sqrt{0.5}, \sqrt{0.5})$	$0.220^{+0.062}_{-0.071}$	$\mathcal{U}(-\sqrt{0.5}, \sqrt{0.5})$
λ [°]	$122.53^{+0.21}_{-5.50}$	$\mathcal{U}(0, 360)$	$230.04^{+0.61}_{-3.53}$	$\mathcal{U}(0, 360)$	$9.93^{+0.55}_{-2.99}$	$\mathcal{U}(0, 360)$
M_{p} [$M_\oplus$]	$3.46^{+0.27}_{-0.97}$	(derived)	$2.24^{+0.13}_{-0.67}$	(derived)	$6.89^{+1.41}_{-0.60}$	(derived)
e	$0.082^{+0.011}_{-0.020}$	$\mathcal{H}_{\mathcal{G}}(0, 0.083)$	$0.0741^{+0.0071}_{-0.0275}$	$\mathcal{H}_{\mathcal{G}}(0, 0.083)$	$0.077^{+0.013}_{-0.031}$	$\mathcal{H}_{\mathcal{G}}(0, 0.083)$
ω [°]	250^{+31}_{-5}	(derived)	194^{+12}_{-13}	(derived)	127^{+16}_{-18}	(derived)
$\mathcal{M}$ [°]	53^{+5}_{-37}	(derived)	216^{+12}_{-14}	(derived)	63^{+16}_{-15}	(derived)
ρ_{p} [$\rho_\oplus$]	$0.426^{+0.013}_{-0.136}$	(derived)	$0.288^{+0.003}_{-0.096}$	(derived)	$0.842^{+0.12}_{-0.123}$	(derived)
ρ_{p} [g cm^{-3}]	$2.339^{+0.073}_{-0.750}$	(derived)	$1.582^{+0.019}_{-0.528}$	(derived)	$4.624^{+0.704}_{-0.676}$	(derived)

	MAP (HDI)	Prior
γ_{RV} [m s^{-1}]	$0.059^{+0.095}_{-0.234}$	$\mathcal{U}(-5005, +5005)$
$\log_2 \sigma_{\mathrm{jitter}}$	-32^{+19}_{-11}	$\mathcal{U}(-49.83, 6.65)$
σ_{jitter} [m s^{-1}]	$\ll 10^{-5}$	(derived)

Notes. All parameters have been defined at the reference time $T_{\mathrm{ref}} = \mathrm{BJD_{TDB}} - 2\,450\,000 = 8379$. $\mathcal{U}(X, Y)$ means uniform distribution between X and Y values; $\mathcal{H}_{\mathcal{G}}(\mu, \sigma)$ means half-normal distribution with mean μ and standard deviation σ.
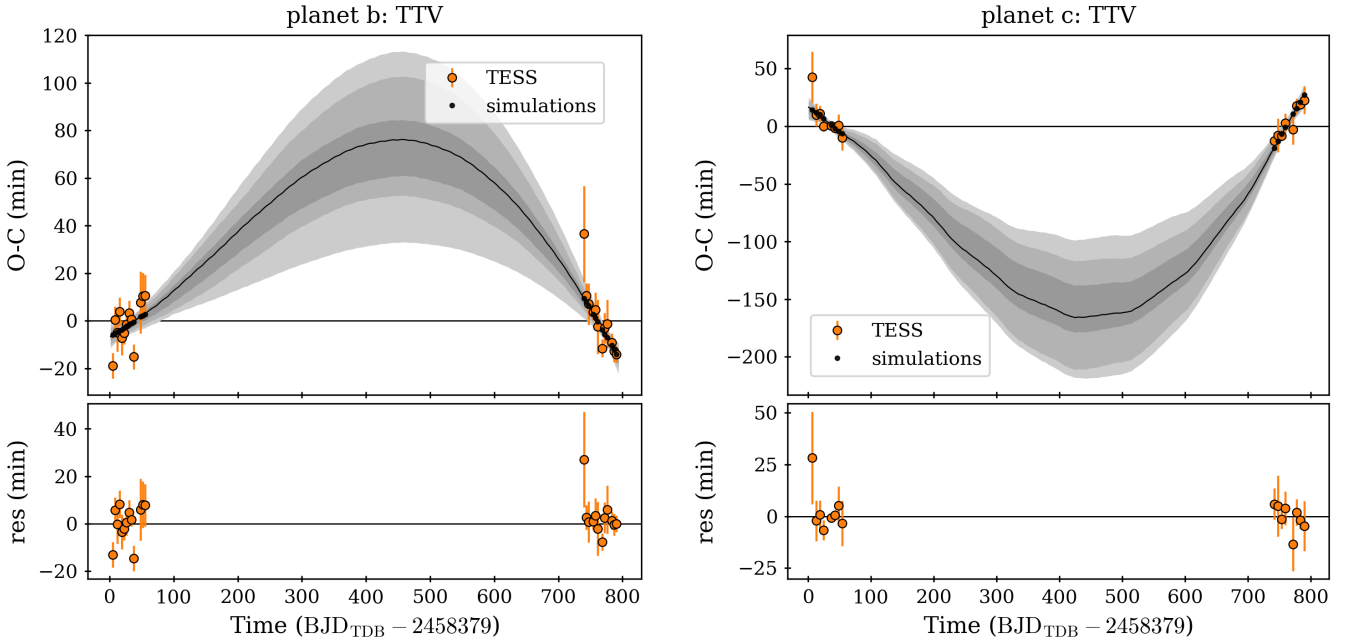

Fig. 6: Observed minus calculated synthetic diagrams derived from the joint RV and TTV dynamical analysis with TRADES for planet b (*left panel*) and c (*right panel*). The $O - C$ for the best-fit (MAP) model is plotted with a black line, while the observed data points are the orange circles. The shaded grey regions displays the confidence intervals at 1, 2, and 3σ, as inferred from the 200 samples randomly drawn from the merged posterior distributions. Residuals are shown in the lower panels.

8. JWST characterisation prospects

All three planets in the TOI-396 system share similar radii ($\sim 2\,R_\oplus$), but span a wide range of masses (0.9–7.1 $M_\oplus$), which

---

[17] https://heasarc.gsfc.nasa.gov/wsgi-scripts/TESS/
TESS-point_Web_Tool/TESS-point_Web_Tool/wtv_v2.0.py/
[18] https://github.com/joannegger/plaNETic

leaves open the question of whether they have primary or secondary atmospheres. Furthermore, the progression of bulk densities with distance from the host star varies in ways that cannot be described by simple formation and evolution models (e.g. Weiss et al. 2018; Mishra et al. 2023).

Given the bright host star and combination of planetary masses, radii, and equilibrium temperatures, the three planets
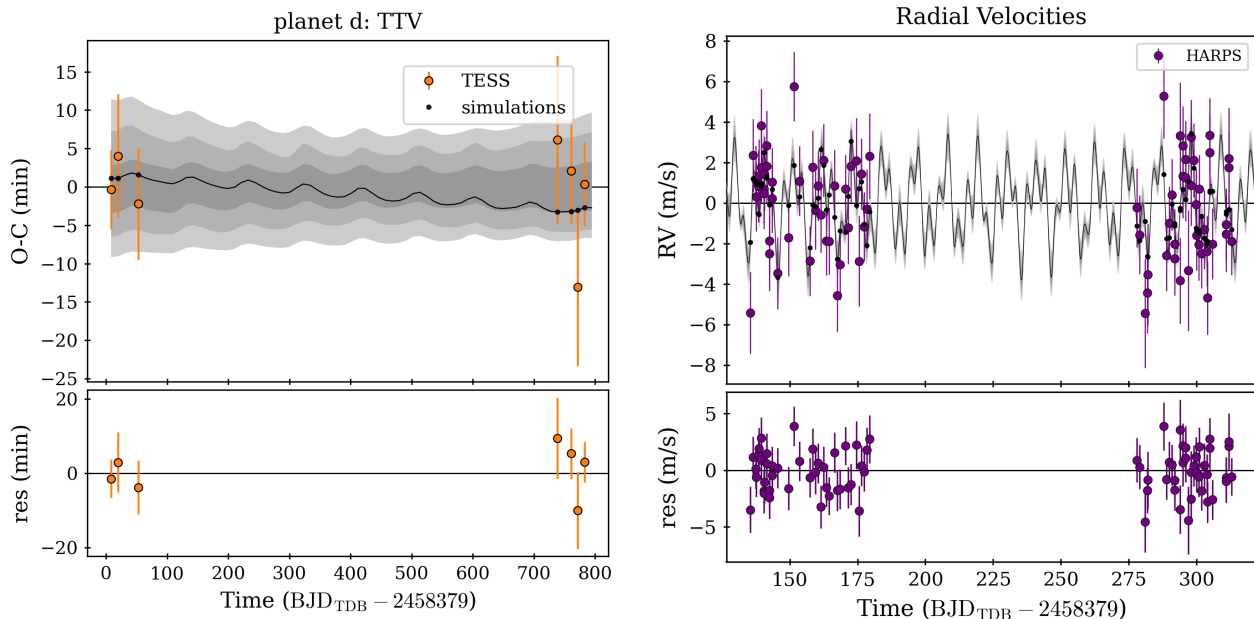
Fig. 7: *Left panel*: Same as Fig. 6, but for TOI-396 d. *Right panel*: Combined RV model of the three planets (black line) superimposed to the de-trended *HARPS* observations (purple circles). The grey shaded area is determined from the 200 sets of system parameters randomly drawn from the merged posterior distributions as obtained from the joint dynamical analysis with TRADES.
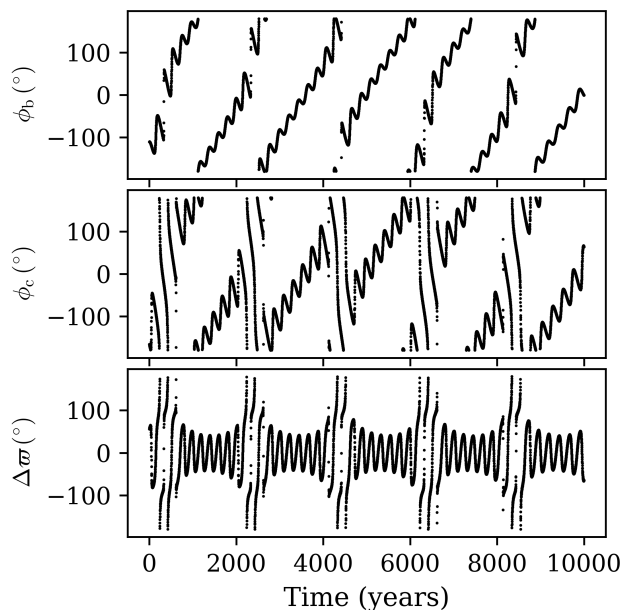

Fig. 8: Temporal evolution of the critical resonance angles ϕ_b (*top panel*) and ϕ_c (*middle panel*) as well as of $\Delta\varpi = (\phi_b - \phi_c)/q$ (*bottom panel*) as inferred when assuming the MAP parameters derived by the TRADES dynamical analysis and integrated with REBOUND+WHFAST for 10 000 years.

have favourable metrics for atmospheric characterisation in both transmission and emission among sub-Neptunes (Kempton et al. 2018, see Fig. 12). This makes the TOI-396 system a highly valuable laboratory to study the formation and evolution of plan-

etary systems. Thus, we explored the prospects for characterisation with JWST. We focused these simulations on emission observations, but we note that transmission and emission have their own advantages and disadvantages in terms of achievable science goals and challenges.

We employed the open-source PYRAT BAY modelling framework (Cubillos & Blecic 2021) to compute synthetic spectra of the TOI-396 planets. These models consist of 1D cloud-free atmospheres in radiative, thermochemical, and hydrostatic equilibrium (Cubillos et al., in prep.). We varied the models' atmospheric elemental content to explore the wide range of compositions that the planets span. For this comparison we settled on two models to represent a primary- and a secondary-atmosphere scenario: the first is a gas giant with a 5× solar metallicity, the second is a water world with a 80% H_2O plus 20% CO_2 composition (based on the C/O ratios seen in the solar system minor bodies, see, e.g., Mumma & Charnley 2011; McKay et al. 2019). For the thermochemical-equilibrium calculations we considered a set of 45 neutral and ionic species, which are the main actors determining the thermal structure. For the radiative-transfer calculation we considered opacities from molecular species for CO, CO_2, CH_4, H_2O, HCN, NH_3, and C_2H_2 from HITEMP and EXOMOL (Rothman et al. 2010; Tennyson et al. 2016); Na and K resonant lines (Burrows et al. 2000); H, H_2, and He Rayleigh (Kurucz 1970); and H_2–H_2 and H_2–He collision-induced absorption (Borysow et al. 2001; Borysow 2002; Richard et al. 2012). We pre-processed the large EXOMOL line lists with the REPACK algorithm (Cubillos 2017) to extract the dominant transitions. Figure 13 (top panels) shows the resulting thermal and composition structure for TOI-396 b (planets c and d follow a similar trend).

The infrared synthetic emission spectra (Fig. 13, bottom panels) are mainly shaped by H_2O, CO_2, and CO features. At most wavelengths the primary- and secondary-atmosphere scenarios roughly differ by an offset, which would be hard to distinguish unless the energy budget of the planets are known. In contrast,
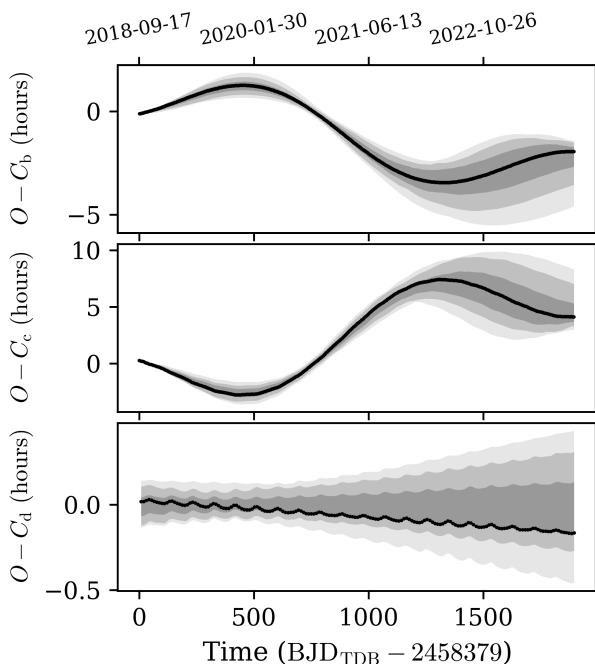
Fig. 9: Synthetic $O - C$ diagrams obtained after performing forward numerical N-body simulations with TRADES (integration of 5.2 years). The C represents the timings calculated from the linear ephemerides in Table 2. The MAP model is plotted with a black line, while the confidence intervals at 1, 2, and 3σ are marked as shaded grey regions and come from 200 random samples drawn from the merged posterior distributions derived from the joint RV and TTV dynamical analysis.

the 4–5 μm window shows the most distinctive spectral features; here the strong CO_2 absorption band at 4.4 μm mainly allows one to distinguish primary from secondary atmospheres. Thus, in the following we focus on this region of the spectrum.

We simulated JWST observations using the PANDEIA exposure time calculator Pontoppidan et al. (2016). The brightness of TOI-396 limits the instrument selection to NIRCam (F444W filter) to avoid saturation. We selected the fastest readout and subarray modes, 5 groups per integration, to optimise the S/N. We generated a distribution of (noised up) realisations for each model to estimate how many eclipses are required to distinguish between primary and secondary atmospheres at the 3σ level. We found that 2, 4, and 8 eclipses (for planets b, c, and d, respectively) would be sufficient to differentiate between these two models. Figure 13 shows one of those random realisations when including the required number of eclipses. The decreasing equilibrium temperature of the planets as they are located further away from TOI-396 plays the major role in the decreasing S/N for planets c and d.

9. Conclusions

The object TOI-396 is an F6 V bright naked-eye star orbited by three planets of almost equal size, and the two inner planets are close to but out of a 5:3 MMR. A photometric analysis of the system was already performed by Vanderburg et al. (2019), but by benefiting from two additional *TESS* sectors, we improved the precision on the planet radii by a factor of ~ 1.4, obtaining $R_b = 2.004^{+0.045}_{-0.047} R_\oplus$, $R_c = 1.979^{+0.054}_{-0.051} R_\oplus$, and $R_d = 2.001^{+0.063}_{-0.064} R_\oplus$.

We determined the masses of the planets by extracting the RV time series from *HARPS* CCFs using an SN fit followed by a joint LC and RV MCMC analysis, where the RV de-trending uses the breakpoint method. We obtained a firm detection of the RV signals of planets b and d, deriving $M_b = 3.55^{+0.94}_{-0.96} M_\oplus$ and $M_d = 7.1 \pm 1.6 M_\oplus$, but we can provide only a 3σ upper limit for the mass of TOI-396 c of $M_c^{\text{up}} = 3.8 M_\oplus$. This yields the following mean planet densities: $\rho_b = 2.44^{+0.69}_{-0.68}$, $\rho_c^{\text{up}} = 2.9$, and $\rho_d = 4.9^{+1.2}_{-1.1}$ g cm^{-3}, implying a quite unusual system architecture (Mishra et al. 2023) where the mid planet is the least dense and the outermost planet is the densest.

The reason for the RV non-detection of any Keplerian signal at $P = P_c \sim 6$ d is likely to be ascribed to the vicinity of P_c to the stellar rotation period. As a matter of fact, from the GLS periodograms of both the RV-related activity indices and the *TESS* raw LCs and from log R'_{HK}-based empirical relations, we consistently inferred $P_{\text{rot},\star} = 6.7 \pm 1.3$ d. After injecting synthetic Keplerian signals at $P = P_{\text{rot},\star}$ and different semi-amplitudes (K_{in}) into the RV time series, we empirically find that the RV semi-amplitudes output by the MCMC analyses (K_{out}) are systematically lower than the input ones by almost 3σ, and they are statistically non-significant as far as $K_{\text{in}} \lesssim K_d$. In addition, we find that $K_{\text{out}} \approx K_c$ when considering a planet with $M_p \sim 3 M_\oplus$ (i.e. $\rho_p \sim 2$ g cm^{-3}), which might correspond to the properties of TOI-396 c. On a more general perspective, these simulations confirm that stellar activity destructively interferes with Keplerian signals having $P \sim P_{\text{rot},\star}$ (e.g. Vanderburg et al. 2016), and furthermore, they indicate that – even in the case of firm detection – values of K_{out} are significantly underestimated.

Longer-baseline RV observations may help disentangle coherent signals originated by Keplerian motions from non-coherent signals due to stellar activity, even if degeneracy issues still hold when the planet orbital period is close to the stellar rotation period (Kossakowski et al. 2022). Alternatively, a possible constraint on M_c may come from TTVs, as planets b and c are close to an MMR of the second order. Indeed, the TTV amplitudes of the two planets show a characteristic anti-correlation pattern, as expected; however, the phase coverage given by the available observations is too poor to perform a conclusive TTV dynamical analysis based on the observed transit timings of the planets. We also attempted to fit the TTV and RV simultaneously while integrating the orbits of the system. We found that the masses and densities of planets b and d are consistent with the results from the joint LC and RV analysis. TOI-396 c shows a dynamical mass of $M_{c,\text{dyn}} = 2.24^{+0.13}_{-0.67} M_\oplus$, which is greater than that inferred from the joint LC and RV analysis, but it is consistent (Z-score = 1.2σ); the density is consistent at the 1.1σ level. However, we emphasise that, although formally precise, the $M_{c,\text{dyn}}$ estimate might not be accurate, as the full coverage of the TTV phase is needed to reliably compute TTV-based masses. Therefore, to fully confirm the system architecture, a reliable estimate of the mass of TOI-396 c is still missing.

We also checked the evolution of the system over 10 000 years, and the critical resonance angles showed that planets b and c are close to but not in a 5:3 MMR. We further performed forward N-body simulations over a temporal baseline of ~ 5.2 years in order to track the transit epochs and evaluate the expected TTV amplitudes during time. It turns out that TOI-396 b and TOI-396 c may exhibit TTVs with a super-period of about 5 years and semi-amplitudes of ~ 2 and ~ 5 hours, respectively. This translates into a temporal drift of the transit timings that can rise up to ~ 5 and ~ 10 hours with respect to the linear ephemerides computed from *TESS* data.
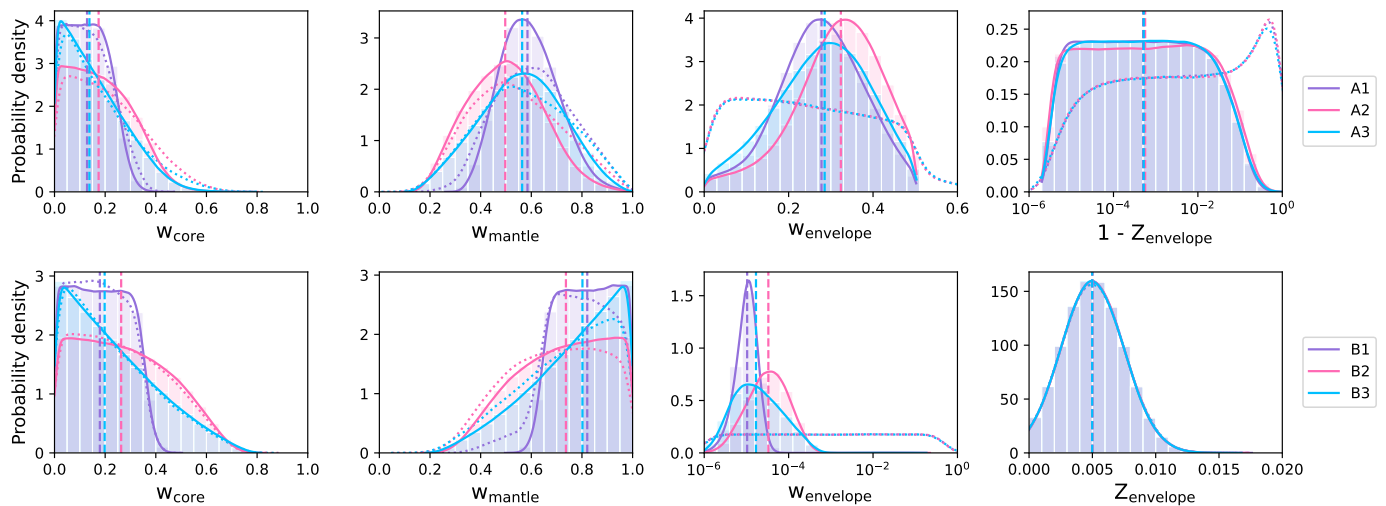
Fig. 10: Inferred posteriors for the most important internal structure parameters of TOI-396 b. The depicted parameters are the mass fractions of the inner core (w_{core}), mantle (w_{mantle}) and envelope layers ($w_{envelope}$) with respect to the total planet mass, and the mass fraction of water in the envelope ($Z_{envelope}$). The top row shows the results when assuming a water prior motivated by a formation of the planet outside the iceline (case A), while the bottom row uses a water prior compatible with a formation inside the iceline (case B). At the same time, we run models with three different compositional priors for the planetary Si/Mg/Fe ratios: stellar (purple, option 1), iron-enriched compared to the star (pink, option 2) and sampled using a uniform prior (blue, option 3). The dotted lines show the prior distributions, while the dashed vertical lines show the median values of the posteriors.
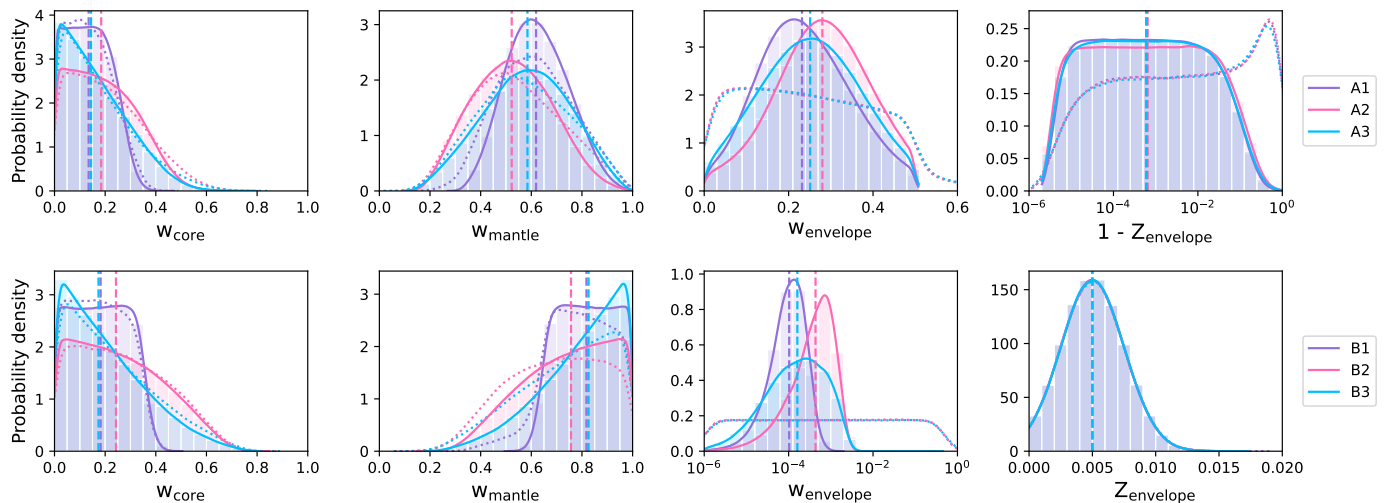

Fig. 11: Same as Figure 10 but for TOI-396 d.

Studying the planetary atmospheres with JWST would take advantage of the favourable spectroscopy metrics of the system (Kempton et al. 2018). Therefore, we set up 1D cloud-free atmospheric models, generated the synthetic emission spectra of the three planets, and simulated eclipse observations with JWST. It turns out that 2, 4, and 8 eclipses (for TOI-396 b, c, and d, respectively) would be sufficient to distinguish between primary and secondary atmosphere scenarios at the 3σ level.

Characterising the nature of the planetary atmosphere is also key to correctly assessing the planetary bulk densities (in particular for planet c). The potentially high TTVs inferred from our simulations should be duly taken into account when scheduling future observations of the target. This holds not only for JWST, but also for *CHEOPS* (Benz et al. 2021), which appears especially suitable for collecting exquisite photometric data to enable the full characterisation of the system.

Fig. 12: Transit (*top panel*) and eclipse (*bottom panel*) spectroscopic metrics for the TOI-396 planets (see legend). The metrics were calculated using the 2MASS Ks-band magnitude. The grey markers show the metrics for the known sample of transiting exoplanets to date. The blue markers show the metrics for targets with approved JWST programmes.
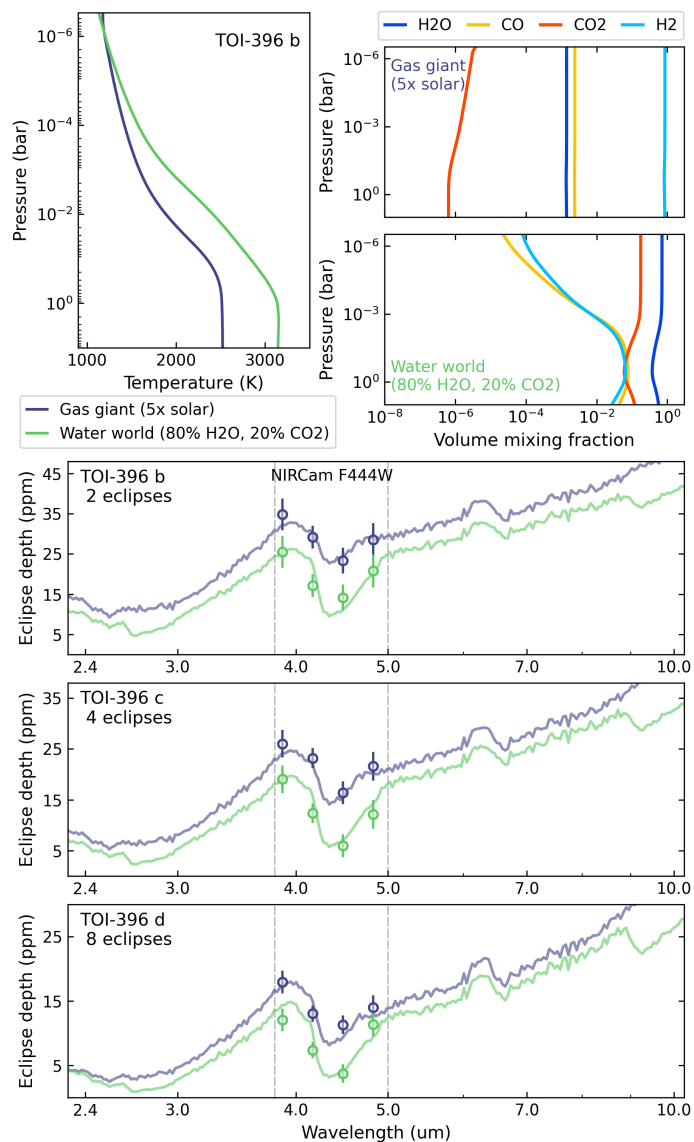
Fig. 13: Simulations of the atmospheric pressure profiles, eclipse spectra, and JWST observations. *Top-left panel*: Radiative-equilibrium thermal profile of TOI-396 b assuming a gas-giant atmosphere (5× solar metallicity) and a secondary atmosphere (80% H_2O plus 20% CO_2). *Top-right panels*: Volume mixing ratio of TOI-396 b for the most relevant species shaping the infrared spectrum. *Bottom panels*: Synthetic secondary eclipse spectra of the three TOI-396 planets (solid curves). The round markers with error bars show a realisation of JWST observation with NIRCam/F444W (and their expected uncertainties) when accumulating 2, 4, and 8 observations for planets b, c, and d, respectively. The vertical dashed lines mark the spectral window covered by NIRCam/F444W.

References

Addison, B., Wright, D. J., Wittenmyer, R. A., et al. 2019, PASP, 131, 115003
Adibekyan, V., Dorn, C., Sousa, S. G., et al. 2021, Science, 374, 330
Adibekyan, V., Figueira, P., Santos, N. C., et al. 2015, A&A, 583, A94
Adibekyan, V. Z., Sousa, S. G., Santos, N. C., et al. 2012, A&A, 545, A32
Agol, E. & Fabrycky, D. C. 2018, in Handbook of Exoplanets, ed. H. J. Deeg & J. A. Belmonte (Cambridge University Press), 7
Agol, E., Steffen, J., Sari, R., & Clarkson, W. 2005, MNRAS, 359, 567
Aguichine, A., Mousis, O., Deleuil, M., & Marcq, E. 2021, ApJ, 914, 84
Alexander, R. D. & Armitage, P. J. 2009, ApJ, 704, 989
Astropy Collaboration, Price-Whelan, A. M., Lim, P. L., et al. 2022, ApJ, 935, 167
Astropy Collaboration, Price-Whelan, A. M., Sipőcz, B. M., et al. 2018, AJ, 156, 123
Astropy Collaboration, Robitaille, T. P., Tollerud, E. J., et al. 2013, A&A, 558, A33
Bai, J. & Perron, P. 2003, Journal of Applied Econometrics, 18, 1
Baranne, A., Queloz, D., Mayor, M., et al. 1996, A&AS, 119, 373
Barnes, S. A. 2010, ApJ, 722, 222
Benz, W., Broeg, C., Fortier, A., et al. 2021, Experimental Astronomy, 51, 109
Bergner, J. B., Öberg, K. I., Bergin, E. A., et al. 2020, ApJ, 898, 97
Bonfanti, A., Delrez, L., Hooton, M. J., et al. 2021, A&A, 646, A157
Bonfanti, A., Gandolfi, D., Egger, J. A., et al. 2023, A&A, 671, L8
Bonfanti, A. & Gillon, M. 2020, A&A, 635, A6
Bonfanti, A., Ortolani, S., & Nascimbeni, V. 2016, A&A, 585, A5
Bonfanti, A., Ortolani, S., Piotto, G., & Nascimbeni, V. 2015, A&A, 575, A18
Borsato, L., Degen, D., Leleu, A., et al. 2024, A&A, 689, A52
Borsato, L., Malavolta, L., Piotto, G., et al. 2019, MNRAS, 484, 3233
Borsato, L., Marzari, F., Nascimbeni, V., et al. 2014, A&A, 571, A38
Borsato, L., Piotto, G., Gandolfi, D., et al. 2021, MNRAS, 506, 3810
Borysow, A. 2002, A&A, 390, 779
Borysow, A., Jorgensen, U. G., & Fu, Y. 2001, J. Quant. Spectr. Rad. Transf., 68, 235
Brasseur, C. E., Phillip, C., Fleming, S. W., Mullally, S. E., & White, R. L. 2019, Astrocut: Tools for creating cutouts of TESS images, Astrophysics Source Code Library, record ascl:1905.007
Bruntt, H., Deleuil, M., Fridlund, M., et al. 2010, A&A, 519, A51
Burrows, A., Marley, M. S., & Sharp, C. M. 2000, ApJ, 531, 438
Ciardi, D. R., Fabrycky, D. C., Ford, E. B., et al. 2013, ApJ, 763, 41
Correia, A. C. M., Delisle, J.-B., & Laskar, J. 2018, in Handbook of Exoplanets, ed. H. J. Deeg & J. A. Belmonte (Springer International Publishing AG, part of Springer Nature), 12
Cubillos, P. E. 2017, ApJ, 850, 32
Cubillos, P. E. & Blecic, J. 2021, MNRAS, 505, 2675
Cutri, R. M., Skrutskie, M. F., van Dyk, S., et al. 2003, 2MASS All Sky Catalog of point sources. (University of Massachusetts and Infrared Processing and Analysis Center (IPAC/California Institute of Technology))
D'Angelo, G. & Lubow, S. H. 2008, ApJ, 685, 560
Delisle, J. B., Laskar, J., Correia, A. C. M., & Boué, G. 2012, A&A, 546, A71
Delrez, L., Ehrenreich, D., Alibert, Y., et al. 2021, Nature Astronomy, 5, 775
Dorn, C., Venturini, J., Khan, A., et al. 2017, A&A, 597, A37
Doyle, A. P., Davies, G. R., Smalley, B., Chaplin, W. J., & Elsworth, Y. 2014, MNRAS, 444, 3592
Dragomir, D., Kane, S. R., Henry, G. W., et al. 2012, ApJ, 754, 37
Dumusque, X., Santos, N. C., Udry, S., Lovis, C., & Bonfils, X. 2011a, A&A, 527, A82
Dumusque, X., Udry, S., Lovis, C., Santos, N. C., & Monteiro, M. J. P. F. G. 2011b, A&A, 525, A140
Egger, J. A., Osborn, H. P., Kubyshkina, D., et al. 2024, A&A, 688, A223
Espinoza, N. & Jordán, A. 2015, MNRAS, 450, 1879
Fabrycky, D. C., Lissauer, J. J., Ragozzine, D., et al. 2014, ApJ, 790, 146
Foreman-Mackey, D., Farr, W., Sinha, M., et al. 2019, The Journal of Open Source Software, 4, 1864
Foreman-Mackey, D., Hogg, D. W., Lang, D., & Goodman, J. 2013, PASP, 125, 306
Fridlund, M., Georgieva, I. Y., Bonfanti, A., et al. 2024, A&A, 684, A12
Gaia Collaboration, Vallenari, A., Brown, A. G. A., et al. 2023, A&A, 674, A1
Gandolfi, D., Barragán, O., Hatzes, A. P., et al. 2017, AJ, 154, 123
Gardner, J. P., Mather, J. C., Clampin, M., et al. 2006, Space Sci. Rev., 123, 485
Gelman, A. & Rubin, D. B. 1992, Statistical Science, 7, 457
Geweke, J. F. 1991, Evaluating the accuracy of sampling-based approaches to the calculation of posterior moments, Staff Report 148, Federal Reserve Bank of Minneapolis
Ginsburg, A., Sipőcz, B. M., Brasseur, C. E., et al. 2019, AJ, 157, 98
Goldreich, P. & Tremaine, S. 1980, ApJ, 241, 425
Goodman, J. & Weare, J. 2010, Communications in Applied Mathematics and Computational Science, 5, 65
Gray, R. O., Corbally, C. J., Garrison, R. F., et al. 2006, AJ, 132, 161

Haldemann, J., Dorn, C., Venturini, J., Alibert, Y., & Benz, W. 2024, A&A, 681, A96
Handberg, R., Lund, M. N., White, T. R., et al. 2021, AJ, 162, 170
Harris, C. R., Millman, K. J., van der Walt, S. J., et al. 2020, Nature, 585, 357
Hatzes, A. P. 2016, in Astrophysics and Space Science Library, Vol. 428, Methods of Detecting Exoplanets: 1st Advanced School on Exoplanetary Science, ed. V. Bozza, L. Mancini, & A. Sozzetti, 3
Hatzes, A. P. 2019, The Doppler Method for the Detection of Exoplanets (Institute of Physics Publishing)
Hatzes, A. P., Dvorak, R., Wuchterl, G., et al. 2010, A&A, 520, A93
Haywood, R. D., Collier Cameron, A., Queloz, D., et al. 2014, MNRAS, 443, 2517
Høg, E., Fabricius, C., Makarov, V. V., et al. 2000, A&A, 355, L27
Holman, M. J., Fabrycky, D. C., Ragozzine, D., et al. 2010, Science, 330, 51
Holman, M. J., Winn, J. N., Latham, D. W., et al. 2006, ApJ, 652, 1715
Hunter, J. D. 2007, Computing in Science & Engineering, 9, 90
Izidoro, A., Ogihara, M., Raymond, S. N., et al. 2017, MNRAS, 470, 1750
Jenkins, J. M., Twicken, J. D., McCauliff, S., et al. 2016, in Society of Photo-Optical Instrumentation Engineers (SPIE) Conference Series, Vol. 9913, Software and Cyberinfrastructure for Astronomy IV, ed. G. Chiozzi & J. C. Guzman, 99133E
Kass, R. E. & Raftery, A. E. 1995, Journal of the American Statistical Association, 90, 773
Kempton, E. M. R., Bean, J. L., Louie, D. R., et al. 2018, PASP, 130, 114401
Kipping, D. M. 2010, MNRAS, 408, 1758
Kossakowski, D., Kürster, M., Henning, T., et al. 2022, A&A, 666, A143
Kuerster, M., Schmitt, J. H. M. M., Cutispoto, G., & Dennerl, K. 1997, A&A, 320, 831
Kurucz, R. L. 1970, SAO Special Report, 309
Kurucz, R. L. 1993, SYNTHE spectrum synthesis programs and line data (Astrophysics Source Code Library)
Kurucz, R. L. 2013, ATLAS12: Opacity sampling model atmosphere program
Laskar, J. 1997, A&A, 317, L75
Laskar, J. 2000, Phys. Rev. Lett., 84, 3240
Laskar, J. & Petit, A. C. 2017, A&A, 605, A72
Lee, M. H. & Peale, S. J. 2002, arXiv e-prints, astro
Leleu, A., Alibert, Y., Hara, N. C., et al. 2021, A&A, 649, A26
Li, M., Huang, S., Petaev, M. I., Zhu, Z., & Steffen, J. H. 2020, MNRAS, 495, 2543
Lightkurve Collaboration, Cardoso, J. V. d. M., Hedges, C., et al. 2018, Lightkurve: Kepler and TESS time series analysis in Python, Astrophysics Source Code Library
Lin, D. N. C. & Papaloizou, J. 1979, MNRAS, 186, 799
Lindegren, L., Bastian, U., Biermann, M., et al. 2021, A&A, 649, A4
Lissauer, J. J., Ragozzine, D., Fabrycky, D. C., et al. 2011, ApJS, 197, 8
Lovis, C. & Pepe, F. 2007, A&A, 468, 1115
Lund, M. N., Handberg, R., Buzasi, D. L., et al. 2021, ApJS, 257, 53
Luque, R., Osborn, H. P., Leleu, A., et al. 2023, Nature, 623, 932
Mamajek, E. E. & Hillenbrand, L. A. 2008, ApJ, 687, 1264
Marigo, P., Girardi, L., Bressan, A., et al. 2017, ApJ, 835, 77
Mayor, M., Pepe, F., Queloz, D., et al. 2003, The Messenger, 114, 20
McKay, A. J., DiSanti, M. A., Kelley, M. S. P., et al. 2019, AJ, 158, 128
Mishra, L., Alibert, Y., Udry, S., & Mordasini, C. 2023, A&A, 670, A68
Morton, T. D. 2012, ApJ, 761, 6
Morton, T. D. 2015, VESPA: False positive probabilities calculator, Astrophysics Source Code Library, record ascl:1503.011
Mumma, M. J. & Charnley, S. B. 2011, ARA&A, 49, 471
Murdoch, K. A., Hearnshaw, J. B., & Clark, M. 1993, ApJ, 413, 349
Nascimbeni, V., Borsato, L., Leonardi, P., et al. 2024, A&A, 690, A349
Nascimbeni, V., Borsato, L., Zingales, T., et al. 2023, A&A, 673, A42
Nelson, B., Ford, E. B., & Payne, M. J. 2014, ApJS, 210, 11
Noyes, R. W., Hartmann, L. W., Baliunas, S. L., Duncan, D. K., & Vaughan, A. H. 1984, ApJ, 279, 763
Otegi, J. F., Bouchy, F., & Helled, R. 2020a, A&A, 634, A43
Otegi, J. F., Dorn, C., Helled, R., et al. 2020b, A&A, 640, A135
Otegi, J. F., Helled, R., & Bouchy, F. 2022, A&A, 658, A107
Parviainen, H., Pallé, E., Nortmann, L., et al. 2016, A&A, 585, A114
Pepe, F., Mayor, M., Galland, F., et al. 2002, A&A, 388, 632
Perryman, M. A. C., Lindegren, L., Kovalevsky, J., et al. 1997, A&A, 323, L49
Persson, C. M., Fridlund, M., Barragán, O., et al. 2018, A&A, 618, A33
Petigura, E. A., Benneke, B., Batygin, K., et al. 2018, AJ, 156, 89
Petigura, E. A., Howard, A. W., Lopez, E. D., et al. 2016, ApJ, 818, 36
Petit, A. C., Laskar, J., & Boué, G. 2018, A&A, 617, A93
Piskunov, N. & Valenti, J. A. 2017, A&A, 597, A16
Piskunov, N. E., Kupka, F., Ryabchikova, T. A., Weiss, W. W., & Jeffery, C. S. 1995, A&AS, 112, 525
Pont, F., Zucker, S., & Queloz, D. 2006, MNRAS, 373, 231

Pontoppidan, K. M., Pickering, T. E., Laidler, V. G., et al. 2016, in Society of Photo-Optical Instrumentation Engineers (SPIE) Conference Series, Vol. 9910, Observatory Operations: Strategies, Processes, and Systems VI, ed. A. B. Peck, R. L. Seaman, & C. R. Benn, 991016

Queloz, D., Henry, G. W., Sivan, J. P., et al. 2001, A&A, 379, 279

Rein, H. & Liu, S. F. 2012, A&A, 537, A128

Rein, H. & Tamayo, D. 2015, MNRAS, 452, 376

Richard, C., Gordon, I. E., Rothman, L. S., et al. 2012, J. Quant. Spectr. Rad. Transf., 113, 1276

Ricker, G. R., Winn, J. N., Vanderspek, R., et al. 2015, Journal of Astronomical Telescopes, Instruments, and Systems, 1, 014003

Rothman, L. S., Gordon, I. E., Barber, R. J., et al. 2010, J. Quant. Spectr. Rad. Transf., 111, 2139

Santos, N. C., Sousa, S. G., Mortier, A., et al. 2013, A&A, 556, A150

Schwarz, G. 1978, Annals of Statistics, 6, 461

Simola, U., Bonfanti, A., Dumusque, X., et al. 2022, A&A, 664, A127

Simola, U., Dumusque, X., & Cisewski-Kehe, J. 2019, A&A, 622, A131

Smith, J. C., Stumpe, M. C., Van Cleve, J. E., et al. 2012, PASP, 124, 1000

Sneden, C. A. 1973, PhD thesis, THE UNIVERSITY OF TEXAS AT AUSTIN.

Sousa, S. G. 2014, in Determination of Atmospheric Parameters of B-, A-, F- and G-Type Stars., ed. E. Niemczura, B. Smalley, & W. Pych (Springer International Publishing (Cham)), 297–310

Sousa, S. G., Adibekyan, V., Delgado-Mena, E., et al. 2021, A&A, 656, A53

Sousa, S. G., Santos, N. C., Adibekyan, V., Delgado-Mena, E., & Israelian, G. 2015, A&A, 577, A67

Sousa, S. G., Santos, N. C., Israelian, G., Mayor, M., & Monteiro, M. J. P. F. G. 2007, A&A, 469, 783

Sousa, S. G., Santos, N. C., Mayor, M., et al. 2008, A&A, 487, 373

Storn, R. & Price, K. 1997, Journal of Global Optimization, 11, 341

Stumpe, M. C., Smith, J. C., Catanzarite, J. H., et al. 2014, PASP, 126, 100

Stumpe, M. C., Smith, J. C., Van Cleve, J. E., et al. 2012, PASP, 124, 985

Suárez Mascareño, A., Rebolo, R., González Hernández, J. I., & Esposito, M. 2017, MNRAS, 468, 4772

Sundman, K. F. 1913, Acta Mathematica, 36, 105

Tanaka, H., Takeuchi, T., & Ward, W. R. 2002, ApJ, 565, 1257

Tennyson, J., Yurchenko, S. N., Al-Refaie, A. F., et al. 2016, Journal of Molecular Spectroscopy, 327, 73

ter Braak, C. J. F. & Vrugt, J. A. 2008, Statistics and Computing, 18, 435

Thiabaud, A., Marboeuf, U., Alibert, Y., et al. 2014, A&A, 562, A27

Thiabaud, A., Marboeuf, U., Alibert, Y., Leya, I., & Mezger, K. 2015, A&A, 574, A138

Trotta, R. 2007, MNRAS, 378, 72

Van Eylen, V., Albrecht, S., Huang, X., et al. 2019, AJ, 157, 61

Vanderburg, A., Huang, C. X., Rodriguez, J. E., et al. 2019, ApJ, 881, L19

Vanderburg, A., Plavchan, P., Johnson, J. A., et al. 2016, MNRAS, 459, 3565

Virtanen, P., Gommers, R., Oliphant, T. E., et al. 2020, Nature Methods, 17, 261

Walsh, C., Nomura, H., & van Dishoeck, E. 2015, A&A, 582, A88

Weiss, L. M. & Marcy, G. W. 2014, ApJ, 783, L6

Weiss, L. M., Marcy, G. W., Petigura, E. A., et al. 2018, AJ, 155, 48

Wildi, F., Pepe, F., Chazelas, B., Lo Curto, G., & Lovis, C. 2010, in Society of Photo-Optical Instrumentation Engineers (SPIE) Conference Series, Vol. 7735, Ground-based and Airborne Instrumentation for Astronomy III, ed. I. S. McLean, S. K. Ramsay, & H. Takami, 77354X

Winn, J. N. 2010, in Exoplanets, ed. S. Seager (University of Arizona Press, Tucson, AZ), 55–77

Winn, J. N. & Fabrycky, D. C. 2015, ARA&A, 53, 409

Wisdom, J. & Holman, M. 1991, AJ, 102, 1528

Zechmeister, M. & Kürster, M. 2009, A&A, 496, 577

[1] Austrian Academy of Sciences, Schmiedlstrasse 6, A-8042 Graz, Austria
e-mail: andrea.bonfanti@oeaw.ac.at

[2] Dipartimento di Fisica, Università degli Studi di Torino, via Pietro Giuria 1, I-10125, Torino, Italy

[3] Department of Physics and Astronomy, Uppsala University, Box 516, Uppsala SE-75120, Sweden

[4] INAF, Osservatorio Astronomico di Padova, Vicolo dell'Osservatorio 5, 35122 Padova, Italy

[5] Weltraumforschung und Planetologie, Physikalisches Institut, University of Bern, Gesellschaftsstrasse 6, 3012 Bern, Switzerland

[6] INAF, Osservatorio Astrofisico di Torino, Via Osservatorio, 20, I-10025 Pino Torinese To, Italy

[7] Department of Physics, University of Warwick, Coventry CV4 7AL, UK

[8] Centre for Exoplanets and Habitability, University of Warwick, Gibbet Hill Road, Coventry CV4 7AL, UK

[9] Departamento de Física Teórica e Experimental, Universidade Federal do Rio Grande do Norte, Campus Universitário, Natal, RN, 59072-970, Brazil

[10] Leiden Observatory, University of Leiden, PO Box 9513, 2300 RA Leiden, The Netherlands

[11] Chalmers University of Technology, Department of Space, Earth and Environment, Onsala Space Observatory, SE-439 92 Onsala, Sweden

[12] INAF-Osservatorio Astrofisico di Arcetri, Largo E. Fermi 5 Florence, Italy

[13] Instituto de Astrofísica e Ciências do Espaço, Universidade do Porto, CAUP, Rua das Estrelas, 4150-762 Porto, Portugal

[14] School of Physics and Astronomy, Physical Science Building, North Haugh, St Andrews, United Kingdom

[15] Rhenish Institute for Environmental Research, Dep. of Planetary Research, University of Cologne, Aachener Str. 209, 50931 Cologne, Germany

[16] Institute of Planetary Research, German Aerospace Center (DLR), Rutherfordstrasse 2, D-12489 Berlin, Germany

[17] Thüringer Landessternwarte Tautenburg, Sternwarte 5, D-07778 Tautenburg, Germany

[18] University Observatory Munich, Ludwig-Maximilians-Universität, Scheinerstr. 1, 81679 Munich, Germany

[19] European Southern Observatory, Alonso de Cordova 3107, Vitacura, Casilla, 19001, Santiago, Chile

[20] European Southern Observatory, Alonso de Cordova 3107, Vitacura, Santiago de Chile, Chile

[21] Centro de Astrobiología (CAB), CSIC-INTA, Camino Bajo del Castillo s/n, 28692, Villanueva de la Cañada (Madrid), Spain

[22] McDonald Observatory, The University of Texas, Austin Texas USA

[23] Center for Planetary Systems Habitability, The University of Texas, Austin Texas

[24] Department of Astronomy & Astrophysics, University of Chicago, Chicago, IL 60637, USA

[25] Astronomy Department and Van Vleck Observatory, Wesleyan University, Middletown, CT 06459, USA

[26] Departamento de Física e Astronomia, Faculdade de Ciências, Universidade do Porto, Rua do Campo Alegre, 4169-007 Porto, Portugal

[27] Department of Astronomy of the University of Geneva, chemin Pegasi 51, 1290 Versoix, Switzerland

[28] Astrobiology Center, NINS, 2-21-1 Osawa, Mitaka, Tokyo 181-8588, Japan

[29] National Astronomical Observatory of Japan, NINS, 2-21-1 Osawa, Mitaka, Tokyo 181-8588, Japan

[30] Astronomical Science Program, Graduate University for Advanced Studies, SOKENDAI, 2-21-1, Osawa, Mitaka, Tokyo, 181-8588, Japan

[31] Instituto de Astrofísica de Canarias (IAC), calle Vía Láctea s/n, 38205 La Laguna, Tenerife, Spain

[32] Departamento de Astrofísica, Universidad de La Laguna (ULL), 38206 La Laguna, Tenerife, Spain

[33] Institute of Astronomy, Faculty of Physics, Astronomy and Informatics, Nicolaus Copernicus University, Grudziądzka 5, 87-100 Toruń, Poland

[34] Department of Physics and Astronomy, McMaster University, 1280 Main St W, Hamilton, ON, L8S 4L8, Canada

[35] Department of Physics, ETH Zurich, Wolfgang-Pauli-Strasse 2, CH-8093 Zurich, Switzerland

Fig. A.1: TTV amplitudes obtained for TOI-396 b (black markers) and TOI-396 c (red markers). This is a superposition of the first two panels of Figure 4 emphasising the anti-correlation pattern.

Appendix A: Supplementary material

Fig. A.2: *Left column*: Generalised Lomb-Scargle periodograms of *TESS* Sector 3 (*first row*), 4 (*second row*), 30 (*third row*), and 31 (*fourth row*) raw photometry. *Right column*: Generalised Lomb-Scargle periodograms of the residuals after removing the best fitting sinusoidal signals at the most significant frequency identified in the periodograms of the corresponding *TESS* time series (left column). The long dashed red line marks the FAP at 0.1%. Significant peaks are detected in the 6—8 day range, which we attribute to the presence of active regions co-rotating with the star.

Table A.1: Radial velocities $\overline{RV}$ as extracted from the centred CCFs with their errors σ_{RV}. They are followed by the hyperparameters inferred from the SN fit onto the CCFs (i.e. $FWHM_{SN}$, A, and γ) and by the bp-detrended RV values (RV_{bp}) with their errors which also account for the jitter ($\sigma_{RV(bp+jitter)}$).

BJD_{TDB}	$\overline{RV}$	σ_{RV}	$FWHM_{SN}$	A	γ	RV_{bp}	$\sigma_{RV(bp+jitter)}$
$[JD - 2\,450\,000]$	$[m\,s^{-1}]$	$[m\,s^{-1}]$	$[km\,s^{-1}]$	$[\%]$		$[m\,s^{-1}]$	$[m\,s^{-1}]$
8514.522079	-3.951	1.406	12.065	27.510	0.0095	-5.358	2.027
8515.519139	3.873	1.058	12.071	27.524	0.0118	2.414	1.803
8516.523282	0.300	0.855	12.064	27.538	0.0109	1.204	1.692
8516.600186	-0.492	0.863	12.064	27.541	0.0117	0.372	1.696
8517.521720	-1.049	1.010	12.055	27.532	0.0105	0.890	1.776
8517.601089	0.374	1.059	12.063	27.540	0.0117	1.412	1.804
8518.527888	1.859	1.021	12.063	27.523	0.0087	1.827	1.782
8518.576207	4.622	1.062	12.072	27.533	0.0084	3.890	1.805
8519.514742	-0.349	0.884	12.066	27.541	0.0103	0.765	1.707
8519.526570	-0.606	0.995	12.066	27.550	0.0080	0.544	1.767
8519.592896	0.359	1.102	12.070	27.549	0.0099	1.506	1.829
8520.511989	2.471	0.962	12.064	27.534	0.0079	2.884	1.748
8520.559451	-0.344	1.093	12.065	27.568	0.0063	1.891	1.824
8521.517823	-2.621	0.854	12.064	27.544	0.0070	-1.799	1.691
8521.563294	-2.900	1.094	12.066	27.541	0.0072	-2.440	1.825
8522.515348	-1.535	0.840	12.067	27.555	0.0085	0.283	1.684
8522.541134	0.229	0.835	12.068	27.551	0.0066	1.106	1.682
8524.539218	-4.858	1.008	12.059	27.543	0.0135	-3.407	1.774
8528.508947	-2.042	1.224	12.062	27.520	0.0087	-1.652	1.905
8530.513044	4.381	0.903	12.063	27.535	0.0090	5.814	1.716
8532.521390	2.482	0.909	12.081	27.544	0.0128	1.143	1.720
8536.503152	-3.627	0.913	12.064	27.529	0.0101	-2.800	1.722
8537.508151	-0.331	1.032	12.050	27.534	0.0068	1.840	1.788
8538.506461	-1.146	1.260	12.068	27.531	0.0044	-0.293	1.929
8539.518544	0.945	0.941	12.064	27.520	0.0101	0.914	1.737
8540.504854	-0.613	1.169	12.057	27.523	0.0065	-0.512	1.870
8541.516591	1.669	1.039	12.072	27.558	0.0079	2.180	1.792
8542.503979	-2.972	0.905	12.067	27.551	0.0098	-1.802	1.718
8543.502941	-4.827	0.781	12.052	27.548	0.0110	-1.815	1.656
8545.522846	-0.012	0.999	12.060	27.550	0.0068	0.913	1.769
8546.513570	-3.846	1.053	12.069	27.547	0.0074	-4.497	1.800
8547.514665	-4.125	0.972	12.064	27.560	0.0081	-2.977	1.754
8549.505689	-1.232	0.824	12.062	27.577	0.0073	0.758	1.676
8550.519298	-0.642	1.050	12.067	27.556	0.0065	-1.147	1.798
8551.501312	-0.164	1.044	12.062	27.571	0.0104	1.877	1.795
8553.499287	3.275	1.525	12.061	27.536	0.0080	2.157	2.111
8554.511465	-0.040	1.684	12.067	27.530	0.0129	-2.804	2.229
8555.493401	2.487	0.982	12.062	27.548	0.0069	1.501	1.760
8556.494019	-5.920	0.876	12.076	27.578	0.0030	-1.109	1.703
8557.489695	0.012	1.313	12.057	27.541	0.0104	-0.227	1.964
8558.510256	3.576	1.523	12.062	27.554	0.0058	2.370	2.110
8656.922558	5.571	1.287	12.065	27.521	0.0096	-0.169	1.946
8657.917377	6.901	1.288	12.087	27.531	0.0074	-1.501	1.947
8659.926600	-1.368	2.267	12.068	27.527	0.0046	-5.376	2.697
8660.912021	-1.737	1.372	12.068	27.544	0.0094	-4.360	2.003

Table A.1: continued.

BJD$_{\text{TDB}}$ [JD $-$ 2 450 000]	$\overline{RV}$ [m s^{-1}]	σ_{RV} [m s^{-1}]	FWHM$_{\text{SN}}$ [km s^{-1}]	A [%]	γ	RV_{bp} [m s^{-1}]	$\sigma_{\text{RV(bp+jitter)}}$ [m s^{-1}]
8660.936119	-0.427	2.037	12.076	27.560	0.0121	-3.455	2.506
8666.907826	6.470	1.514	12.078	27.534	0.0104	5.351	2.104
8667.940719	-3.649	0.960	12.075	27.554	0.0093	-2.530	1.747
8668.949085	-8.977	1.057	12.076	27.552	0.0028	-0.924	1.802
8669.932275	-1.509	1.000	12.076	27.572	0.0055	0.474	1.770
8670.877547	-3.853	1.101	12.066	27.551	0.0048	-2.679	1.829
8670.943987	-2.070	0.934	12.074	27.566	0.0071	-1.958	1.733
8672.892348	2.329	1.552	12.073	27.495	0.0071	-3.765	2.131
8672.937224	6.039	2.184	12.066	27.493	0.0111	3.382	2.627
8673.885378	3.408	1.281	12.077	27.544	0.0092	2.900	1.942
8673.953311	9.563	1.450	12.080	27.534	0.0132	1.387	2.058
8674.893561	4.520	1.229	12.075	27.549	0.0080	2.229	1.908
8674.952407	6.129	1.587	12.074	27.516	0.0080	1.317	2.156
8675.896534	-0.472	2.590	12.069	27.541	0.0086	-3.271	2.973
8676.890399	7.142	1.127	12.055	27.536	0.0086	3.314	1.844
8676.931698	4.179	1.359	12.063	27.545	0.0084	0.939	1.994
8677.940205	4.018	1.075	12.076	27.551	0.0093	2.179	1.813
8678.854134	4.830	0.960	12.069	27.544	0.0078	0.004	1.747
8678.914902	2.784	0.925	12.067	27.547	0.0081	-1.534	1.729
8679.872861	3.456	1.000	12.067	27.523	0.0089	-1.987	1.770
8679.934961	4.891	0.831	12.071	27.532	0.0093	0.768	1.680
8680.893592	-0.225	0.902	12.077	27.551	0.0098	-2.422	1.716
8681.884748	5.537	1.281	12.064	27.528	0.0082	-1.250	1.943
8682.859272	-7.039	0.944	12.075	27.550	0.0020	-2.313	1.738
8682.939961	2.124	1.076	12.073	27.540	0.0067	-4.614	1.814
8683.875650	4.838	1.197	12.083	27.564	0.0094	2.553	1.888
8683.908141	6.550	1.150	12.082	27.560	0.0090	3.403	1.858
8684.816283	-0.252	0.967	12.076	27.559	0.0106	-1.949	1.751
8689.838032	3.280	1.025	12.072	27.556	0.0075	-1.000	1.784
8689.929566	-6.178	1.172	12.066	27.527	0.0018	-1.467	1.872
8690.851088	6.751	0.946	12.064	27.542	0.0062	1.820	1.740
8690.940875	6.573	2.035	12.059	27.530	0.0051	2.266	2.504
8691.920653	-0.563	0.781	12.093	27.551	0.0088	-1.822	1.656

Table A.2: Polynomial detrending baseline applied to the *TESS* LCs within the MCMC scheme.

Light curve	Planet	Detrending
TE 1	b	$t^2 + pc2^1$
TE 2	c	$t^3 + pc1^2 + (xy)^1$
TE 3	b d	c
TE 4	b c	c
TE 5	b	$t^3 + pc1^1$
TE 6	c	c
TE 7	b d	t^1
TE 8	b	$t^1 + pc2^1$
TE 9	c	t^1
TE 10	b	t^1
TE 11	b	$t^4 + pc2^1$
TE 12	b	$t^3 + pc2^2$
TE 13	c	$t^2 + pc2^1$
TE 14	b	c
TE 15	c	$t^2 + pc2^1 + (xy)^1$
TE 16	b	c
TE 17	c	t^1
TE 18	b	$t^4 + pc2^1$
TE 19	d	t^2
TE 20	c	$t^4 + pc2^1$
TE 21	b	c
TE 22	d	c
TE 23	b	c
TE 24	c	c
TE 25	b	c
TE 26	b c	c
TE 27	c	c
TE 28	b	$pc2^1$
TE 29	b	c
TE 30	c	$t^1 + pc1^2$
TE 31	d	$pc1^2 + (xy)^1$
TE 32	b	$pc2^1$
TE 33	b	c
TE 34	c	t^1
TE 35	b d	t^1
TE 36	b	$pc1^1$
TE 37	c	t^2
TE 38	b c d	$pc1^1$
TE 39	b	$pc1^1$
TE 40	c	t^1
TE 41	b	t^1

Notes. *TESS* (TE) LCs are identified by a counter based on the chronological order of observation. In particular, LCs from 1 to 11, from 12 to 21, from 22 to 32, and from 33 to 41 were extracted from Sector 3, 4, 30, and 31, respectively. c indicates a normalisation scalar; see text for further details.

Table A.3: Timing of each transit event T_{tr} and the corresponding TTV amplitude as computed with respect to linear ephemerides. The last column specifies the *TESS* sector where the transit occurs.

TOI-396 b		
T_{tr} [BJD]	TTV [min]	Sector
$8384.0799^{+0.0035}_{-0.0037}$	$-18.9^{+5.0}_{-5.3}$	3
$8387.6787^{+0.0038}_{-0.0033}$	$+0.5^{+5.4}_{-4.7}$	3
$8391.2602^{+0.0057}_{-0.0056}$	$-4.8^{+8.2}_{-8.1}$	3
8394.8516 ± 0.0040	$+4.0 \pm 5.8$	3
$8398.4292^{+0.0051}_{-0.0041}$	$-7.2^{+7.3}_{-5.9}$	3
$8402.0159^{+0.0029}_{-0.0033}$	$-5.1^{+4.1}_{-4.8}$	3
$8405.6036^{+0.0036}_{-0.0038}$	$-1.6^{+5.1}_{-5.5}$	3
$8409.1923^{+0.0036}_{-0.0034}$	$+3.2^{+5.2}_{-4.9}$	3
$8412.7757^{+0.0019}_{-0.0017}$	$+0.5^{+2.7}_{-2.5}$	4
$8416.3501^{+0.0023}_{-0.0037}$	$-15.1^{+3.2}_{-5.3}$	4
$8427.1218^{+0.0091}_{-0.0041}$	$+8^{+13}_{-6}$	4
$8430.7089^{+0.0068}_{-0.0037}$	$+10.3^{+9.8}_{-5.3}$	4
$8434.2944^{+0.0062}_{-0.0050}$	$+10.6^{+5.2}_{-3.5}$	4
$9119.102^{+0.004}_{-0.014}$	$+37^{+6}_{-20}$	30
$9122.6695^{+0.0036}_{-0.0024}$	$+10.6^{+5.2}_{-3.5}$	30
$9126.2523^{+0.0060}_{-0.0044}$	$+7.0^{+8.6}_{-6.3}$	30
$9133.4205^{+0.0023}_{-0.0015}$	$+3.6^{+3.3}_{-2.2}$	30
$9137.0065^{+0.0051}_{-0.0031}$	$+4.7^{+7.3}_{-4.4}$	30
$9140.5868^{+0.0056}_{-0.0079}$	-3^{+8}_{-11}	30
$9147.7511^{+0.0026}_{-0.0025}$	$-11.5^{+3.7}_{-3.6}$	31
$9151.3423^{+0.0045}_{-0.0031}$	$-3.1^{+6.4}_{-4.4}$	31
$9154.9289^{+0.0046}_{-0.0071}$	-1^{+7}_{-10}	31
$9162.0940^{+0.0024}_{-0.0027}$	$-9.1^{+3.4}_{-3.8}$	31
$9165.6768^{+0.0025}_{-0.0032}$	$-12.7^{+3.6}_{-4.6}$	31
$9169.2611^{+0.0016}_{-0.0024}$	$-14.1^{+2.4}_{-3.4}$	31

TOI-396 c		
T_{tr} [BJD]	TTV [min]	Sector
$8385.794^{+0.010}_{-0.016}$	$+43^{+15}_{-22}$	3
$8391.7447^{+0.0068}_{-0.0063}$	$+9.7^{+9.8}_{-9.1}$	3
$8397.7195^{+0.0046}_{-0.0047}$	$+11.0^{+6.6}_{-6.8}$	3
8403.6857 ± 0.0033	$0.0^{+4.7}_{-4.8}$	3
$8415.6337^{+0.0015}_{-0.0013}$	$+0.4^{+2.2}_{-1.9}$	4
$8421.6062^{+0.0017}_{-0.0016}$	$-1.7^{+2.5}_{-2.3}$	4
$8427.5817^{+0.0065}_{-0.0033}$	$+0.7^{+9.4}_{-4.7}$	4
$8433.5482^{+0.0042}_{-0.0077}$	-10^{+6}_{-11}	4
$9120.5407^{+0.0052}_{-0.0043}$	$-12.8^{+7.5}_{-6.3}$	30
9126.518 ± 0.010	-8^{+14}_{-15}	30
$9132.4916^{+0.0032}_{-0.0020}$	$-8.2^{+4.5}_{-2.9}$	30
$9138.4731^{+0.0057}_{-0.0040}$	$+2.8^{+8.2}_{-5.7}$	30
$9150.4169^{+0.0085}_{-0.0090}$	-3^{+12}_{-13}	31
$9156.4050^{+0.0029}_{-0.0044}$	$+17.6^{+4.2}_{-6.4}$	31
$9162.3798^{+0.0027}_{-0.0030}$	$+19.0^{+3.8}_{-4.4}$	31
$9168.3562^{+0.0068}_{-0.0084}$	$+23^{+10}_{-12}$	31

TOI-396 d		
$8387.2711^{+0.0036}_{-0.0034}$	$-0.4^{+5.2}_{-4.9}$	3
$8398.5047^{+0.0056}_{-0.0051}$	$4.0^{+8.1}_{-7.4}$	3
$8432.1919^{+0.0050}_{-0.0034}$	$-2.2^{+7.2}_{-4.9}$	4
$9117.2589^{+0.0076}_{-0.0068}$	$+6^{+11}_{-10}$	30
$9139.7171^{+0.0047}_{-0.0025}$	$+2.1^{+6.8}_{-3.6}$	30
$9150.9371^{+0.0072}_{-0.0037}$	-13^{+10}_{-5}	31
$9162.1769^{+0.0038}_{-0.0031}$	$+0.3^{+5.5}_{-4.5}$	31

Table A.4: Results of the internal structure modelling for TOI-396 b. The 'w.' symbol represents the mass fraction with respect to the total planet mass, $Z_{envelope}$ is the water mass fraction in the planet envelope, while the 'x.' symbol represents the molar fraction of a given chemical element either in the planet core ($x_{.,core}$) or in the mantle ($x_{.,mantle}$).

Water prior	Formation outside iceline (water-rich)			Formation inside iceline (water-poor)		
Si/Mg/Fe prior	Stellar (A1)	Iron-enriched (A2)	Free (A3)	Stellar (B1)	Iron-enriched (B2)	Free (B3)
w_{core} [%]	$12.8^{+9.1}_{-8.7}$	$17.4^{+14.3}_{-12.0}$	$13.8^{+15.1}_{-9.9}$	$17.9^{+12.4}_{-12.2}$	$26.3^{+21.4}_{-18.1}$	$19.8^{+22.4}_{-14.3}$
w_{mantle} [%]	$58.5^{+12.4}_{-10.8}$	$49.7^{+15.3}_{-15.3}$	$56.4^{+16.5}_{-17.5}$	$82.1^{+12.2}_{-12.4}$	$73.7^{+18.1}_{-21.4}$	$80.2^{+14.3}_{-22.4}$
$w_{envelope}$ [%]	$27.8^{+10.1}_{-10.1}$	$32.4^{+12.4}_{-11.0}$	$28.5^{+10.8}_{-12.5}$	$\left(1.0^{+0.7}_{-0.5}\right) 10^{-3}$	$\left(3.3^{+6.7}_{-2.3}\right) 10^{-3}$	$\left(1.7^{+6.0}_{-1.2}\right) 10^{-3}$
$Z_{envelope}$ [%]	$99.9^{+0.0}_{-1.5}$	$99.9^{+0.1}_{-1.8}$	$99.9^{+0.1}_{-1.5}$	$0.5^{+0.2}_{-0.2}$	$0.5^{+0.2}_{-0.2}$	$0.5^{+0.2}_{-0.2}$
$x_{Fe,core}$ [%]	$90.3^{+6.5}_{-6.4}$	$90.4^{+6.5}_{-6.4}$	$90.4^{+6.5}_{-6.4}$	$90.3^{+6.5}_{-6.4}$	$90.4^{+6.5}_{-6.4}$	$90.3^{+6.5}_{-6.4}$
$x_{S,core}$ [%]	$9.7^{+6.4}_{-6.5}$	$9.6^{+6.4}_{-6.5}$	$9.6^{+6.4}_{-6.5}$	$9.7^{+6.4}_{-6.5}$	$9.6^{+6.4}_{-6.5}$	$9.7^{+6.4}_{-6.5}$
$x_{Si,mantle}$ [%]	$38.7^{+7.3}_{-6.2}$	$32.5^{+10.2}_{-9.2}$	$34.3^{+29.2}_{-23.2}$	$38.6^{+7.3}_{-6.1}$	$32.1^{+10.4}_{-9.2}$	$32.6^{+29.2}_{-22.5}$
$x_{Mg,mantle}$ [%]	$42.5^{+7.8}_{-7.1}$	$35.4^{+11.4}_{-10.5}$	$35.6^{+29.1}_{-24.2}$	$42.5^{+7.9}_{-7.1}$	$35.1^{+11.5}_{-10.5}$	$35.9^{+29.4}_{-24.1}$
$x_{Fe,mantle}$ [%]	$18.6^{+9.7}_{-12.0}$	$31.2^{+19.1}_{-20.0}$	$22.2^{+23.4}_{-15.7}$	$18.8^{+9.6}_{-12.1}$	$31.9^{+19.0}_{-20.2}$	$23.2^{+23.9}_{-16.6}$

Table A.5: Same as Tab. A.4, but for TOI-396 d.

Water prior	Formation outside iceline (water-rich)			Formation inside iceline (water-poor)		
Si/Mg/Fe prior	Stellar (A1)	Iron-enriched (A2)	Free (A3)	Stellar (B1)	Iron-enriched (B2)	Free (B3)
w_{core} [%]	$13.5^{+9.6}_{-9.2}$	$18.4^{+15.2}_{-12.7}$	$14.4^{+15.8}_{-10.3}$	$18.2^{+12.3}_{-12.4}$	$24.3^{+21.1}_{-16.8}$	$17.4^{+20.2}_{-12.5}$
w_{mantle} [%]	$61.9^{+13.2}_{-11.9}$	$52.3^{+16.5}_{-16.2}$	$58.5^{+17.2}_{-18.2}$	$81.8^{+12.4}_{-12.3}$	$75.7^{+16.8}_{-21.1}$	$82.6^{+12.5}_{-20.2}$
$w_{envelope}$ [%]	$23.2^{+11.9}_{-10.3}$	$28.0^{+11.0}_{-11.3}$	$25.1^{+12.2}_{-12.2}$	$\left(1.0^{+1.4}_{-0.7}\right) 10^{-2}$	$\left(4.3^{+6.6}_{-3.3}\right) 10^{-2}$	$\left(1.6^{+6.0}_{-1.4}\right) 10^{-2}$
$Z_{envelope}$ [%]	$99.9^{+0.1}_{-1.8}$	$99.9^{+0.1}_{-2.2}$	$99.9^{+0.1}_{-1.8}$	$0.5^{+0.2}_{-0.2}$	$0.5^{+0.2}_{-0.2}$	$0.5^{+0.2}_{-0.2}$
$x_{Fe,core}$ [%]	$90.3^{+6.5}_{-6.4}$	$90.4^{+6.5}_{-6.4}$	$90.3^{+6.5}_{-6.4}$	$90.3^{+6.6}_{-6.4}$	$90.4^{+6.5}_{-6.4}$	$90.3^{+6.5}_{-6.4}$
$x_{S,core}$ [%]	$9.7^{+6.4}_{-6.5}$	$9.6^{+6.4}_{-6.5}$	$9.7^{+6.4}_{-6.5}$	$9.7^{+6.4}_{-6.6}$	$9.6^{+6.4}_{-6.5}$	$9.7^{+6.4}_{-6.5}$
$x_{Si,mantle}$ [%]	$38.7^{+7.3}_{-6.2}$	$32.4^{+10.2}_{-9.2}$	$33.9^{+29.1}_{-22.9}$	$38.7^{+7.3}_{-6.2}$	$32.9^{+10.2}_{-9.3}$	$35.7^{+28.8}_{-24.3}$
$x_{Mg,mantle}$ [%]	$42.5^{+7.8}_{-7.0}$	$35.4^{+11.5}_{-10.5}$	$35.6^{+29.1}_{-24.2}$	$42.6^{+7.8}_{-7.1}$	$36.0^{+11.3}_{-10.7}$	$36.5^{+30.3}_{-25.2}$
$x_{Fe,mantle}$ [%]	$18.7^{+9.7}_{-12.0}$	$31.4^{+19.0}_{-20.0}$	$22.5^{+23.4}_{-15.9}$	$18.6^{+9.8}_{-11.9}$	$30.2^{+19.4}_{-19.6}$	$19.9^{+22.6}_{-14.3}$